

1 **Inhibition of mixed-layer deepening during winter**  
2 **in the northeastern Arabian Sea by the**  
3 **West India Coastal Current**

4 **D. Shankar · R. Remya ·**  
5 **P. N. Vinayachandran · Abhisek**  
6 **Chatterjee · Ambica Behera**

7 the date of receipt and acceptance should be inserted later

8 **Abstract** Though the deep mixed layers (MLs) that form in the northeast-  
9 ern Arabian Sea (NEAS) during the winter monsoon (November–February)  
10 have been attributed to convective mixing driven by dry, cool northeasterly

---

D. Shankar · R. Remya

CSIR-National Institute of Oceanography, Dona Paula, Goa 403004, India

E-mail: shankar@nio.org

D. Shankar · R. Remya

Academy of Scientific and Innovative Research (AcSIR), CSIR-NIO, Goa, India

P. N. Vinayachandran

Indian Institute of Science, Bengaluru, India

A. Chatterjee

ESSO-Indian National Centre for Ocean Information Services, Hyderabad, India

Ambica Behera

Indian Institute of Science, Bengaluru, India

---

11 winds from the Indian subcontinent, data show that the deepest MLs occur  
12 in the northern NEAS and the maxima of latent-heat and net heat fluxes in  
13 the southern NEAS. We use an oceanic general circulation model to show that  
14 the deep MLs in the NEAS extend up to  $\sim 20^\circ\text{N}$  till the end of December,  
15 but are restricted poleward of  $\sim 22^\circ\text{N}$  ( $\sim 23^\circ\text{N}$ ) in January (February). This  
16 progressive restriction of the deep mixed layers within the NEAS is due to  
17 poleward advection of water of lower salinity by the West India Coastal Cur-  
18 rent (WICC). The deep MLs are sustained till February in the northern NEAS  
19 because convective mixing deepens the ML before the waters of lower salinity  
20 reach this region and the wind stirring and convective overturning generate suf-  
21 ficient turbulent energy for the ML to maintain the depth attained in January.  
22 Though the atmospheric fluxes tend to cool the ML in the southern NEAS,  
23 this cooling is countered by the warming due to horizontal advection. Likewise,  
24 the cooling due to entrainment, which continues in the southern NEAS even as  
25 the ML shallows during January–February, is almost cancelled by the warm-  
26 ing caused by a downwelling vertical velocity field. Therefore, the SST changes  
27 very little during December–February even as the ML shallows dramatically  
28 in the southern NEAS. These deep MLs of the NEAS also preclude a strong  
29 intraseasonal response to the intraseasonal variability in the fluxes. This role  
30 of horizontal advection implies that the ML depth in the NEAS is determined  
31 by an interplay of physical processes that are forced differently. The convective  
32 mixing depends on processes that are local to the region, but the advection is  
33 due to the WICC, whose seasonal cycle is primarily forced by remote winds.

34 By inhibiting the formation of deep MLs in the southern NEAS, the WICC  
35 limits the region of formation of the high-salinity water masses of this region.  
36 Since the deep MLs in the NEAS have been linked to the high chlorophyll  
37 concentration there, our results imply that the conventional approach of av-  
38 eraging over boxes for studying the impact of physics on biogeochemistry can  
39 mask important details that are due to advection because it is the advective  
40 component of any budget that is most affected by the averaging process.

41 **Keywords:** Mixed layer; Ocean dynamics; Turbulent mixing; Eastern bound-  
42 ary current; Indian Ocean; Chlorophyll; Monsoon; Biogeochemistry.

## 43 1 Introduction

44 The seasonally reversing winds over the north Indian Ocean (NIO; north of  
45 5°S) drive a seasonally reversing circulation. This seasonality of the physical  
46 forcing leads to two phytoplankton growing seasons, one each during the sum-  
47 mer monsoon (June–September; also called “southwest” monsoon) and win-  
48 ter monsoon (November–February; also called “northeast” monsoon) (Banse  
49 1987). The link between the physical forcing and phytoplankton blooms has  
50 been the subject of several observational and modelling studies in the Arabian  
51 Sea, the western arm of the NIO (see, for example, Banse 1968, 1984, 1987;  
52 Madhupratap et al 1996; McCreary et al 1996, 2001, 2009; Wiggert et al 2000,  
53 2002, 2005, 2006, 2009; Lévy et al 2007; Koné et al 2009; Hood et al 2009;  
54 Gomes et al 2014). There exist significant regional differences, as noted by  
55 several authors, in the timing and extent of these blooms, but the importance

56 of the physical forcing has been highlighted by all (Banse 1987; Naqvi 1991;  
57 Naqvi et al 2006; Lévy et al 2007; McCreary et al 2009; Wiggert et al 2009;  
58 Koné et al 2009).

59 Observations and models show that in the eastern Arabian Sea (EAS) (Fig-  
60 ure 1), there is a difference in the phytoplankton blooms between the southern  
61 and northern parts (Figure 2). Off the southern part of the Indian west coast,  
62 a bloom occurs only during the summer monsoon, when the mixed layer (ML)  
63 shallows as a consequence of upwelling; in contrast, the northeastern Arabian  
64 Sea (NEAS) shows two distinct blooms, one each during the summer and win-  
65 ter monsoons (Banse 1987; Lévy et al 2007; McCreary et al 2009; Koné et al  
66 2009). The summer bloom in the NEAS has also been attributed to upwelling  
67 (Banse 1968, 1987; Lévy et al 2007; McCreary et al 2009; Koné et al 2009).  
68 The EAS is one of the three major upwelling regimes of the Arabian Sea,  
69 the other two occurring off Somalia and Oman (see, for example, Banse 1968,  
70 1984; McCreary et al 1993; Schott and McCreary 2001).

71 The productivity of the NEAS during winter was tentatively attributed  
72 initially to upwelling because of the existence of a cross-shore temperature  
73 gradient with the warmer waters occurring offshore (Carruthers et al 1959),  
74 but Banse (1968) noted the absence of regular upwelling in the region during  
75 November–February. It is Banse (1968) who first pointed to the possibility  
76 of the lower sea surface temperatures (SSTs) observed in the NEAS during  
77 winter being a consequence of wind-driven surface cooling. The tide-gauge sea-  
78 level data in the EAS show a climatological maximum during winter (Banse

79 1984; Shetye and Almeida 1985), suggesting a poleward geostrophic boundary  
80 current that cannot favour upwelling during this season off the Indian west  
81 coast (Banse 1968, 1984; Sharma 1968; Pankajakshan and Ramaraju 1987;  
82 Shetye and Shenoi 1988). It was realised by this time that the large-scale  
83 boundary current in the EAS, the West India Coastal Current (WICC) (Shetye  
84 et al 1990, 1991a; McCreary et al 1993; Shankar and Shetye 1997; Shetye and  
85 Gouveia 1998; Schott and McCreary 2001; Shankar et al 2002) flowed poleward  
86 into the local alongshore wind during winter (see Amol et al 2014, for a brief  
87 history of the WICC literature), prompting Banse (1984) to suggest a role for  
88 the large-scale circulation in the forcing of the winter WICC.

89 All studies that we are aware of attribute the higher productivity and  
90 phytoplankton bloom in the NEAS during winter to this convective mixing  
91 that entrains nutrients into the surface ML as it deepens (Banse 1968, 1984,  
92 1987; Madhupratap et al 1996; Lévy et al 2007; McCreary et al 2009; Koné et al  
93 2009; Gomes et al 2014), and available data suggest that this proposed link  
94 between the deep ML (Chatterjee et al 2012) and the chlorophyll concentration  
95 (Lévy et al 2006) is viable, with the higher chlorophyll concentration tending  
96 to be co-located with the deeper ML during winter (Figure 3). The chlorophyll  
97 bloom peaks in February (Lévy et al 2007), following the peak in the ML depth  
98 (MLD) (Figure 3).

99 The dry, cool northeasterly winds blowing onto the sea from land are  
100 expected to cool the surface of the NEAS. All these studies (Banse 1968,  
101 1984, 1987; Shetye et al 1992; McCreary et al 1993, 2009; Prasannakumar

102 and Prasad 1996, 1999; Madhupratap et al 1996; Lévy et al 2007; Koné et al  
103 2009; Gomes et al 2014) invoke the increase in latent-heat flux, a consequence  
104 of the northeasterly winds being both strong and dry, and the decrease in  
105 incoming shortwave flux during winter as the cause of the deep MLs. The  
106 increased evaporation is expected to lead to a decrease in surface tempera-  
107 ture and an increase in the surface salinity and density, leading to convective  
108 mixing and the formation of one of the three high-salinity water masses of  
109 the NIO (Rochford 1964; Banse 1968, 1984; Wyrтки 1971; Shetye et al 1992;  
110 Shenoi et al 1993; Prasannakumar and Prasad 1999). This high-salinity water  
111 mass is characteristic of the northern Arabian Sea and has been called the  
112 Arabian Sea High-Salinity Water (ASHSW) mass (Rochford 1964). Modelling  
113 studies have validated this hypothesis of water-mass formation by deep con-  
114 vective mixing (McCreary et al 1993; Han 1999; Han et al 2001; Prasad and  
115 Ikeda 2002b,a; Lévy et al 2007; Koné et al 2009) and suggest that it forms  
116 over a broad region. The hydrographic data show that salinity decreases below  
117 the ML (Rochford 1964; Wyrтки 1971; Varma et al 1980; Shetye et al 1992;  
118 Shenoi et al 1993); this intermediate layer of lower salinity, which would imply  
119 an unstable water column if it were not for a sharp decrease in temperature at  
120 the base of the ML to counter the haline effect, has been called the Arabian  
121 Sea Salinity Minimum (Shenoi et al 1993).

122 While all these studies invoke deep convective mixing as the cause of the  
123 deep MLs, their spatial focus has been constrained by the availability of data.  
124 Much of the literature even for the northern Arabian Sea is therefore restricted

125 to the region sampled by the international and Indian JGOFS (Joint Global  
126 Ocean Flux Study) programmes of the mid-1990s (Prasannakumar and Prasad  
127 1996; Madhupratap et al 1996; Wiggert et al 2000, 2002, 2005). None of these  
128 JGOFS cruises sampled the region of deep MLs in the northernmost Arabian  
129 Sea (Figure 3), for which most of the data available are from the International  
130 Indian Ocean Expedition (IIOE) of the 1960s (Wyrski 1971; Levitus 1982;  
131 Locarnini et al 2010; Antonov et al 2010; Chatterjee et al 2012) and two  
132 cruises during the 1970s (Varma et al 1980; Banse and Postel 2009). The  
133 more recent data are largely due to Argo floats and an examination of the  
134 distribution of hydrographic profiles shows an extremely sparse distribution  
135 of data in the northern NEAS (see Figures 1, 20, and 21 in Chatterjee et al  
136 2012), which accounts for the deepest mixed layers. The ASHSW forming in  
137 this region sinks to a depth greater than does the ASHSW formed farther  
138 south in the NEAS (Naqvi et al 2006) and was therefore distinguished as the  
139 Northern Arabian Sea High-Salinity Water (NASHSW) mass by Banse and  
140 Postel (2009).

141 Curiously, however, observations show that the regimes of the deepest MLs  
142 (Varma et al 1980; Banse and Postel 2009; Chatterjee et al 2012) and the high-  
143 est latent-heat flux (Praveenkumar et al 2012) do not coincide (Figure 4): the  
144 deepest MLs are in the northernmost part of the NEAS, where the NASHSW  
145 forms, but the highest latent-heat flux occurs farther to the south, where the  
146 winds are stronger, but the ML is thinner and the water mass that forms is the  
147 ASHSW. The sensible-heat flux (all fluxes in Figure 4 are from Praveenkumar

148 et al (2012)) is higher in the north, but this flux is almost an order of mag-  
149 nitude smaller than the latent-heat flux. The net longwave flux varies more  
150 cross-shore than alongshore. The net shortwave flux into the ocean is less in  
151 the northern NEAS, complementing the latent-heat flux, but the net flux out  
152 of the ocean during January is still higher in the southern NEAS. A similar  
153 discrepancy between the fluxes and deep MLs is seen during February.

154 That the deepest MLs do not coincide with the highest latent-heat flux and  
155 that the spatial differences in MLD are not matched by similar gradients in the  
156 net flux out of the ocean suggests that processes other than convective mixing  
157 driven by local winds are also important. Though Naqvi et al (2006) state that  
158 “the lower salinity and higher temperature of the water derived from the south  
159 do not permit sufficient densification to trigger convective mixing, except in  
160 the most northern parts”, a quantitative study of the impact of advection  
161 has not been carried out. The simulations of Han et al (2001) suggest that  
162 evaporation affects the MLD in the NEAS and that the effect is not uniform  
163 in space, but their study dealt with the entire Indian Ocean and therefore did  
164 not quantify the processes specifically for the NEAS.

165 In this paper, we use an oceanic general circulation model (OGCM) to  
166 investigate the factors that determine the MLD during winter in the NEAS,  
167 which we define as the region east of 64°E and north of 18°N (Figure 1).  
168 Though the high chlorophyll concentration in the NEAS provides the motiva-  
169 tion for this study, our focus in this paper is restricted to the physical processes  
170 determining the spatio-temporal variation of MLD within the NEAS during



171 the winter monsoon. We show that the deep MLs in the NEAS extend up  
172 to  $\sim 20^\circ\text{N}$  till the end of December, but are restricted poleward of  $\sim 22^\circ\text{N}$   
173 ( $\sim 23^\circ\text{N}$ ) in January (February). This progressive restriction of the deep mixed  
174 layers within the NEAS is due to poleward advection of water of lower salin-  
175 ity by the boundary current, the WICC. We also show that the decrease in  
176 MLD in the southern NEAS, particularly large in February, is not matched  
177 by a corresponding change in the SST. The paper is organised as follows. In  
178 Section 2, we present the model details. The evolution of the model ML in  
179 the NEAS during winter is presented in Section 3 and the role of advection is  
180 analysed in Section 4. Section 5 concludes the paper.

## 181 **2 The model**

182 Our OGCM is version MOM4p1 of MOM (Modular Ocean Model) (Griffies  
183 2009), configured for the Indian Ocean as in Kurian and Vinayachandran  
184 (2007), Vinayachandran et al (2007), and Chatterjee et al (2013). A detailed  
185 description of the model setup is given in Chatterjee et al (2013) and we pro-  
186 vide but an overview here.

187 MOM has a free surface and uses the hydrostatic approximation. The hor-  
188 izontal resolution in our setup is  $0.25^\circ \times 0.25^\circ$  and there are 40 vertical levels,  
189 with 25 levels in the top 200 m and a 5-m resolution in the top 60 m. The model  
190 domain extends over the Indian Ocean ( $30^\circ\text{--}120^\circ\text{E}$ ,  $30^\circ\text{S--}30^\circ\text{N}$ ). Bottom to-  
191 pography is based on a modified ETOPO2 bathymetry (Sindhu et al 2007),  
192 with the minimum ocean depth set to 15 m and isolated land points (i. e.,

single cells) removed. The Palk Strait between India and Sri Lanka is closed, and the outflow regions of the Red Sea and Persian Gulf are broadened and deepened to ensure smooth flow between these narrow channels and the Arabian Sea. At land boundaries, a no-flux condition is imposed for tracers and no-slip and no-normal-flow conditions are imposed for velocity. Sponge layers of width  $3.5^\circ$  are applied to the open southern ( $30^\circ\text{S}$ ) and eastern ( $120^\circ\text{E}$ ) boundaries, where tracer fields are relaxed to climatological values (Chatterjee et al 2012) with a time scale of 30 days; no restoration is applied to the tracer fields elsewhere in the model domain. The Chatterjee et al (2012) climatology adds data within the Indian Exclusive Economic Zone (EEZ) from Indian sources to the data set that was used to prepare the temperature and salinity climatologies of the World Ocean Atlas (Locarnini et al 2010; Antonov et al 2010); inclusion of these Indian data leads to significant improvement in the climatology within the Indian EEZ by presenting more stable climatological values. The model physics and parameterisation choices are listed in Table 1.

Sources for the model forcing are listed in Table 2. River discharge, based on the data set of Vörösmarty et al (1996), is specified in the top two layers of the vertical grid; the discharge for the Ganga and Brahmaputra, which have the highest discharge into the NIO, is, however, based on the more recent data set from Papa et al (2010). Most of the forcing is from the OMIP (Ocean Model Inter-comparison Project) (Röske 2001) data set. The OMIP data, which constitute a daily climatology, are derived from ECMWF (European Centre for Medium-range Weather Forecasting) Reanalysis for 1979–1993

216 (Gibson et al 1997) and provide a consistent forcing set that has been used  
217 for inter-comparison of model forecasts. The model ocean was spun up from a  
218 state of rest for 14 years and the results presented are for the 15th year.

219 The model simulation has been validated earlier for the NIO (Kurian and  
220 Vinayachandran 2007; Vinayachandran et al 2007) and equatorial IO (Chat-  
221 terjee et al 2013) and we restrict our model validation to monthly climatologies  
222 of MLD, SST, and sea-surface salinity (SSS). (Unless otherwise stated, SST  
223 and SSS refer to the temperature and salinity, respectively, of the ML.) Clima-  
224 tological observed MLD is calculated from the Chatterjee et al (2012) data set  
225 using a density criterion: the MLD is defined as the depth at which the density  
226 increase from the surface surface corresponds to a  $0.5^{\circ}\text{C}$  decrease in tempera-  
227 ture (Shenoi et al 2004). The model MLD is defined as the depth at which the  
228 buoyancy difference with respect to the surface level is equal to  $0.0003 \text{ m s}^{-2}$   
229 (Kurian and Vinayachandran 2007). (Computing the model MLD with the  
230 criterion used by Chatterjee et al (2012) leads to a difference of but a few  
231 metres, which is inconsequential for the results of this paper. Hence, we stick  
232 to the more commonly used MLD criterion for MOM.)

233 The model simulation compares well with the observations (Figure 5). As  
234 noted by Kurian and Vinayachandran (2007), the model WICC matches that  
235 observed (Mariano et al 1995). For validating SST, we compare the model sim-  
236 ulation with TMI (TRMM Microwave Imager; TRMM: Tropical Rainfall Mea-  
237 suring Mission). The model SST is within  $0.5^{\circ}\text{C}$  of the observations through-  
238 out the year over the model domain even without flux correction (Kurian and

239 Vinayachandran 2007), but the model is cooler in the NEAS throughout the  
240 winter monsoon. For salinity, the only data set available is based on hydrog-  
241 raphy and one must remember that the salinity data are extremely sparse in  
242 the NEAS (Chatterjee et al 2012). The model simulates a lower salinity than  
243 observed, but the alongshore salinity variation, important for this analysis, is  
244 simulated fairly well. Without any artificial methods like salinity relaxation,  
245 the southeastern Arabian Sea (SEAS) freshens at the same time as in the  
246 observations and the poleward advection of low-salinity waters off the Indian  
247 west coast is more striking than in the observations (Kurian and Vinayachan-  
248 dran 2007). This role of advection in determining the spatial variation of SSS  
249 is evident in the model, whose finer resolution ( $0.25^\circ \times 0.25^\circ$  compared to  
250  $1^\circ \times 1^\circ$  for the observed climatology) makes it possible to see clearly the low-  
251 salinity tongue, due to the WICC, separating the higher-salinity waters on the  
252 shelf from the higher-salinity waters offshore of the WICC (Figure 5). In the  
253 NEAS, the model simulates a deeper ML than observed and the deep MLs  
254 extend farther south in the model than in the observations, but the spatio-  
255 temporal variation of MLD within the NEAS is evident in both observations  
256 and model. The correlations between the modelled and observed MLD, SST,  
257 and SSS for the NEAS are 0.78, 0.92, and 0.65, respectively (0.83, 0.89, and  
258 0.64, respectively) during October–March (full year); all these correlations are  
259 significant at the 99% level. (The SST correlations are for the model and  
260 TMI; the MLD and SSS correlations are for the model and the climatology of  
261 Chatterjee et al (2012).)

### 262 **3 Evolution of the mixed layer in the NEAS during winter**

#### 263 3.1 Evolution of the mixed layer and air-sea fluxes

264 The annual range of SST (model ML temperature) in the NEAS is  $\sim 6^\circ\text{C}$ . SST  
265 falls below  $26.5^\circ\text{C}$  in the northern NEAS (north of  $23^\circ\text{N}$ ) during November  
266 and the  $26^\circ\text{C}$  contour extends equatorward to  $19.5^\circ\text{N}$  along the continental  
267 slope (marked by the 1000 m isobath) in December (Figure 5). SST decreases  
268 inshore and the coolest waters are near the coast, as noted earlier (Carruthers  
269 et al 1959). SST decreases in the NEAS till February, but the difference at  
270  $22^\circ\text{N}$  from December–February is just  $\sim 1.5^\circ\text{C}$ . The warming of the NEAS  
271 starts in March.

272 SSS (model ML salinity) is expected to increase during winter as a conse-  
273 quence of the evaporative cooling, but remains almost constant during October–  
274 November. SSS remains practically constant — its value hovers around 36.4 psu  
275 (practical salinity unit) — during November–January in the north and off-  
276 shore, away from the regime of the narrow WICC (Figure 5). Farther south,  
277 however, SSS at  $22^\circ\text{N}$  on the 1000 m isobath decreases from 36.3 to 35.9 psu  
278 from November to February.

279 The model ML starts deepening after October, but the MLD in the NEAS  
280 on the continental slope is still of the order of 30 m in November. It is during  
281 this transition period that the WICC reverses direction (Shetye and Shenoi  
282 1988; McCreary et al 1993; Shetye and Gouveia 1998; Schott and McCreary  
283 2001) (Figure 5). In December, the ML deepens beyond 80 m in patches on

284 the continental shelf and deepens to  $\sim 90$  m on the continental slope (just  
285 offshore of the 1000 m isobath); the deepening of the ML in December is  
286 almost uniform all along the continental slope poleward of  $\sim 20^\circ\text{N}$  (Figure 5).  
287 In this regime of the NEAS, the ML continues to deepen through January,  
288 but the deepening is much greater north of  $\sim 22^\circ\text{N}$  ( $\sim 140$  m) than between  
289  $20$ – $22^\circ\text{N}$  ( $\sim 90$  m). In February, the ML shallows in the southern NEAS to  
290  $\sim 60$  m and the regime of shallow MLs extends up to  $\sim 23^\circ\text{N}$ ; poleward of  
291  $\sim 23^\circ\text{N}$ , the region of deep MLs extends farther offshore than in January. In  
292 March (figure not shown), the ML shallows all over the NEAS.

293        Though the deeper MLs occur north of  $22$ – $23^\circ\text{N}$  (Figure 5), the net heat  
294 flux out of the ocean is less north of  $23^\circ\text{N}$  (Figure 6), implying weaker convec-  
295 tive mixing. As may be expected, the longwave and sensible-heat fluxes do not  
296 vary significantly with latitude in the NEAS, and the north-south difference  
297 in net heat flux is essentially determined by the latent-heat and shortwave  
298 fluxes (Figure 6). Throughout this paper, positive values imply fluxes out of  
299 the ocean. Though the shortwave flux into the ocean decreases poleward, the  
300 latent-heat flux is less poleward of  $\sim 23^\circ\text{N}$ , i.e., in the northern NEAS, during  
301 December–January. As a consequence of this distribution of the air-sea fluxes  
302 on the continental slope, the net heat flux during December is  $\sim 20$  W m<sup>2</sup>  
303 higher at  $21^\circ\text{N}$  compared to  $24^\circ\text{N}$ , implying stronger convective mixing in  
304 the southern NEAS. In February, the shortwave flux increases all over the  
305 NEAS, but the difference in net heat flux between the northern and southern

306 NEAS changes sign, with the outgoing flux at 24°N exceeding that at 21°N  
307 by  $\sim 20 \text{ W m}^2$ .

### 308 3.2 The questions

309 The evolution of the ML during winter in the NEAS leads to three questions.  
310 First, substantial deepening of the ML is highly localised even within the  
311 NEAS and does not coincide with the high latent-heat or net heat fluxes out  
312 of the ocean. Therefore, the question is why the ML shallows in the southern  
313 NEAS even as it continues to deepen in the north after December? The second  
314 question is a corollary of the first question: what sustains the deep ML in  
315 the northern NEAS during February? Third, even as the MLD undergoes  
316 large changes in the southern NEAS during January–February, the SST barely  
317 changes. Naqvi et al (2006) suggested that the relatively shallower ML in the  
318 southern NEAS is due to the poleward advection of fresher and warmer water  
319 by the WICC. Since the SST does increase from north to south (Figure 5),  
320 implying that the WICC will advect warmer waters poleward, and the net heat  
321 flux out of the ocean decreases all over the NEAS from January to February  
322 (Figure 6), why does the SST not increase at least in the southern NEAS? The  
323 analysis carried out in the rest of this paper is aimed at answering these three  
324 questions. We begin by analysing the contribution of the winds (momentum  
325 fluxes) and buoyancy fluxes to the spatio-temporal variation in the MLD.

---

 326 3.3 Mixed-layer physics

327 When the ML shallows, the Monin-Obukhov depth (Monin and Obukhov 1954)  
 328 is often used to describe the balance between the turbulent kinetic energy  
 329 (TKE) input by the momentum fluxes due to the wind and the buoyancy fluxes  
 330 in the ML. The idea is that if the TKE input by the wind is not sufficient to  
 331 maintain the MLD when the buoyancy fluxes are negative (equivalent to a  
 332 heat gain at the ocean surface according to the sign convention used in this  
 333 paper), then the ML shallows to the Monin-Obukhov depth,  $H_{MO}$  (Kraus and  
 334 Turner 1967; Qiu and Kelly 1993; McCreary et al 1996; Han et al 2001; Rao  
 335 et al 2002). Production of TKE is given by (following Han et al 2001; Rao  
 336 et al 2002)

$$P_{TKE} = \rho u_*^3 + \rho \kappa H_{MO} B_0, \quad (1)$$

337 where  $\rho$  is the density of sea water ( $1026 \text{ kg m}^{-3}$ ),  $\kappa = 0.42$  is the von Kärman  
 338 constant (Rao et al 2002),  $u_* = \sqrt{\frac{\tau}{\rho}}$  is the friction velocity (with  $\tau$  the mag-  
 339 nitude of the wind stress),  $g$  is the acceleration due to gravity, and

$$B_0 = 0.5g \left[ -\frac{\alpha Q_0}{\rho C_p} + \beta(E - P)S_0 \right] \quad (2)$$

340 is the depth-averaged buoyancy flux (unit  $\text{m}^2 \text{ s}^{-3}$ ) (Han et al 2001; Cronin  
 341 and Sprintall 2001). Note that the buoyancy flux of the ML is given by  $B_0 H$ ,  
 342 where  $H$  is the MLD. In Equation (2),  $C_p$  is the specific heat constant (at  
 343 constant pressure) for sea water,  $Q_0$  is the net heat flux out of the marine  
 344 boundary layer (positive out of the ocean, so that a positive  $Q_0$  will tend to  
 345 deepen the ML),  $E$  is the evaporation rate,  $P$  is the precipitation rate,  $S_0$  is



346 the salinity of the ML, and  $\alpha = -0.00025 \text{ K}^{-1}$  and  $\beta = 0.00785 \text{ psu}^{-1}$  are the  
 347 thermal expansion coefficient and haline contraction coefficient, respectively.  
 348 Note that the  $Q_0 = Q_{\text{net}} - Q_d$ , where  $Q_{\text{net}}$  is the net heat flux at the ocean  
 349 surface and  $Q_d$  is the shortwave heat flux lost at the bottom of the mixed layer  
 350 (the penetrative heat flux), and that this description of the heat budget does  
 351 not include advection, which, as we shall see, makes a significant contribution  
 352 to the heat budget of the ML in the NEAS.

353 The first term on the RHS of Equation (1) represents the production of  
 354 TKE by wind stirring and the second term the sum of thermal and haline  
 355 buoyancy fluxes. The wind-stirring term, by definition, cannot be negative;  
 356 hence, a balance between the two terms, leading to  $P_{\text{TKE}} = 0$  and a physically  
 357 realistic or positive  $H_{\text{MO}}$ , is possible only when the buoyancy flux is negative,  
 358 implying a net heat gain by the ocean and/or an excess of precipitation over  
 359 evaporation. When this balance holds,

$$H_{\text{MO}} = -\frac{u_*^3}{\kappa B_0}. \quad (3)$$

360 In the NEAS, evaporation exceeds precipitation throughout the winter  
 361 monsoon, implying a positive buoyancy flux due to the haline component.  
 362 Therefore, a change of sign in the buoyancy flux can only come from the ther-  
 363 mal buoyancy component. The thermal buoyancy flux in this region is an order  
 364 of magnitude greater than the term representing turbulent energy generated  
 365 by the winds (Figure 7). The shallowing of the ML from February to March  
 366 is due to a negative thermal buoyancy flux, a consequence of the increase in  
 367 solar radiation leading to a net heat flux into the ocean. This negative ther-

mal buoyancy flux overwhelms the smaller haline buoyancy flux, leading to a physically sensible, i. e., positive,  $H_{MO}$  at the end of the winter monsoon.

In contrast, the shallowing of the ML in the southern NEAS from January to February is not associated with a negative thermal buoyancy flux (Figure 7). Indeed, the net heat flux is out of the ocean over almost the entire NEAS during February (Figure 6), leading to a positive thermal buoyancy flux. Therefore, the buoyancy flux (Figure 7) supports convective overturning throughout the winter monsoon and implies a negative (physically meaningless)  $H_{MO}$ . Comparison of the pattern of MLD and buoyancy fluxes (thermal, haline, and total) during January–February shows an almost perfect match, suggesting a close relation between the two variables. Since the buoyancy fluxes include MLD (i. e., the buoyancy flux is the product of  $B_0$  and the MLD in Equation (1)), this match is not surprising. A plot of the depth-averaged buoyancy fluxes (i. e.,  $B_0$ ) shows that the spatial scale over which these quantities (or even the surface buoyancy fluxes) vary is much larger (Figure 8), as may be expected from the similar spatial scales for the net heat flux from January to February (Figure 6).

This striking difference between the large-scale changes in the depth-averaged buoyancy fluxes and the much more slope-trapped pattern of the buoyancy fluxes implies that there is more to the spatial and temporal variation of the MLD in the NEAS than merely the convective mixing invoked in the literature. The wedge-shaped intrusion, from south to north, of fresher water along the continental slope separates waters of higher salinity on the shelf and farther

391 offshore of this wedge created by the WICC (Figure 5); this role of the WICC  
392 has been suggested earlier (Prasannakumar and Prasad 1999; Han et al 2001;  
393 Naqvi et al 2006), and we analyse it in the following section.

#### 394 **4 Role of advection**

395 To quantify the role of advection, it is necessary to recognise that the WICC  
396 hugs the continental slope (Shetye et al 1991a) (Figure 5). This boundary  
397 current propagates offshore as a Rossby wave on seasonal time scales (Mc-  
398 Creary et al 1993; Shankar and Shetye 1997; Shankar et al 2002, 2010), but it  
399 narrows poleward (Shetye et al 1991a) because the phase speed of the west-  
400 ward propagating Rossby wave decreases as the square of the distance from  
401 the equator. Even at  $10^{\circ}\text{N}$ , the theoretical and observed Rossby-wave speed  
402 for the first baroclinic mode is  $\sim 10 \text{ cm s}^{-1}$  (Shankar et al 2004), implying  
403 a speed of  $\sim 2 \text{ cm s}^{-1}$  in the NEAS. Hence, the WICC propagates offshore  
404 slowly enough in the NEAS to permit an analysis of the role of advection  
405 by considering the spatio-temporal variability along the 1000 m isobath; the  
406 model grid cells used in these figures are shown in Figure 1.

407 A plot of the model variables along the 1000 m isobath (henceforth referred  
408 to as alongshore variation) shows that the WICC reverses at the end of Oc-  
409 tober and the ML deepens uniformly poleward of  $\sim 19.5^{\circ}\text{N}$  during November  
410 (Figure 9). This situation persists through December, except for the extreme  
411 north of the NEAS, i. e., on the continental slope off the southern coast of Pak-  
412 istan, where the ML deepens more than in the rest of the NEAS. In January,

413 the distinction between the northern and southern NEAS becomes more strik-  
414 ing, with the ML deepening to over 130 m (less than 100 m) north (south) of  
415  $\sim 22^\circ\text{N}$ . The distinguishing latitude shifts poleward to  $\sim 23^\circ\text{N}$  and the along-  
416 shore gradient of MLD increases in February, when the ML shallows (deepens)  
417 to  $\sim 60$  m ( $\sim 140$  m) in the southern (northern) NEAS. This north-south dif-  
418 ference in MLD disappears in the second half of March as the ML shallows to  
419 almost 40 m all over the NEAS. This shallowing in March is a consequence  
420 of the increase in net shortwave flux (into the ocean), which overwhelms the  
421 latent-heat and longwave fluxes, leading to a classical detrainment (Kraus and  
422 Turner 1967; McCreary et al 1996, 2009) situation.

423 The latitudinal dependence of SST becomes evident in December (Fig-  
424 ure 9). Note that the SST contours in the figure are almost flat from mid-  
425 December (mid-January) to the end of February in the southern (northern)  
426 NEAS, implying that SST barely changes even as the ML shallows (deepens) in  
427 February in the southern (northern) NEAS. The variation of SSS is in contrast  
428 to that of SST: except for the regime north of  $\sim 24^\circ\text{N}$ , where the SSS is rela-  
429 tively constant through November–March, it decreases almost monotonically  
430 through December–February and the lower salinities extend farther poleward  
431 with time. There is a striking match between the variation of MLD (100–110 m  
432 contours) and SSS (36.10 psu contour), suggesting that it is the decrease in  
433 SSS, rather than a change in SST, that leads to the rapid shallowing of the  
434 ML south of  $\sim 23^\circ\text{N}$  during February.

435 The role of the WICC in decreasing the salinity along the continental slope  
436 is evident in an analysis of the salt budget for the ML (Figure 10). Atmospheric  
437 forcing tends to increase salinity because evaporation exceeds precipitation,  
438 but it is more than compensated by the freshening due to the advection of  
439 waters of lower salinity from the south. Except for a few bursts (these in-  
440 traseasonal bursts have a time scale of the order of a week) during November  
441 and February–March, the sub-surface processes (essentially entrainment and  
442 vertical advection; figure not shown) make but a meagre contribution to the  
443 salt budget of the ML. Hence, the ML shallows in the southern NEAS owing  
444 to the inflow of lower-salinity waters from the south.

445 A similar analysis of the heat budget of the ML (Figure 11) shows a dom-  
446 inance of atmospheric forcing, with the significant contribution of horizontal  
447 advection restricted equatorward of  $19^{\circ}\text{N}$  till the end of January. The short-  
448 wave flux is dominated by a seasonal cycle, but the latent-heat and long-  
449 wave fluxes exhibit intraseasonal bursts (Figure 12). As with the salt budget,  
450 the sub-surface processes have a small effect on the ML temperature because  
451 the contributions of vertical advection and entrainment mixing tend to cancel  
452 throughout the winter monsoon (Figure 13). Vertical advection tends to warm,  
453 rather than cool, the mixed layer because the vertical velocity is negative, i.e.,  
454 downwelling-favourable. An exception is a relatively strong warming burst due  
455 to vertical advection at the end of October.

456 Though the WICC advects low-salinity waters poleward into the northern  
457 NEAS as well, the ML remains deep till the end of February because it deep-

458 ens to over 100 m before the inflow of low-salinity water can decrease the ML  
459 salinity (Figure 9). The buoyancy fluxes and the TKE due to the wind are  
460 sufficient (Figure 14) to maintain the MLD at over 100 m until the shortwave  
461 radiation increases and latent-heat flux decreases in March (Figure 12), en-  
462 abling the ML to detrain and shallow to a depth of  $\sim 40$  m by the end of the  
463 month (Figure 9).

464 The role of vertical advection, which tends to warm the ML because of  
465 downwelling, has largely been ignored in the literature. The downwelling in  
466 the NEAS, primarily forced by remote winds through the poleward propaga-  
467 tion of Kelvin waves that lower the thermocline and raise sea level along the  
468 west coast of India during the winter monsoon (McCreary et al 1993; Shankar  
469 and Shetye 1997; Shankar 1998, 2000; Shankar et al 2002), counters the cool-  
470 ing due to entrainment of cooler, sub-surface waters. A consequence of these  
471 contrasting influences is that SST, or the ML temperature, is almost constant  
472 through January–February even as the ML shallows owing to the poleward ad-  
473 vection of low-salinity waters by the WICC. The inflow of low-salinity water  
474 at the surface increases the vertical salinity gradient at the base of the mixed  
475 layer (Figure 15): the gradient, which was negative because of the Arabian  
476 Sea Salinity Minimum underlying the ASHSW in the ML (Shenoi et al 1993)  
477 before November, turns positive as the ML shallows south of  $23^{\circ}\text{N}$  in January–  
478 February. As a result of this intrusion of low-salinity water at the surface, a  
479 weak barrier layer (Lukas and Lindström 1991; Vialard and Delecluse 1998)  
480 forms and the vertical temperature gradient weakens to near-zero values at

481 the base of the mixed layer (Figure 15). Therefore, the SST does not decrease  
482 in the southern NEAS in spite of the net heat flux being out of the ocean  
483 (Figure 6) and the positive buoyancy fluxes (Figure 14) therefore tending to  
484 deepen the ML. That the flux is still out of the ocean in February permits  
485 a balance between the cooling by air-sea fluxes and the warming due to the  
486 inflow of warmer water. Therefore, the SST remains almost constant even as  
487 the ML shallows by  $\sim 50$  m from January to February.

## 488 **5 Discussion**

489 In summary, we have used an OGCM to investigate the climatological spatio-  
490 temporal variability of the depth of the mixed layer in the NEAS during the  
491 winter monsoon. A description of this variability led to three questions.

492 The first question was the cause of the shallowing of the ML during January–  
493 February in the southern NEAS even as it continued to deepen in the north  
494 (Figures 5 and 9). Earlier hypotheses suggested that this difference between the  
495 northern and southern NEAS was due to the poleward advection of warmer,  
496 fresher waters by the WICC (Naqvi et al 2006). Our simulations show that it  
497 is the salinity that is important: the alongshore salinity gradient in the eastern  
498 Arabian Sea, a consequence of the freshening in the south and excess of evap-  
499 oration over precipitation in the north (Shetye et al 1991a; Levitus 1982; Han  
500 et al 2001; Antonov et al 2010; Chatterjee et al 2012) implies that the poleward  
501 WICC stabilises the water column (Figure 15). In contrast to this freshening  
502 of the ML, its temperature, or the SST, barely changes during December–

503 February, ruling out a similar impact due to the advection of warmer waters  
504 from the south.

505 The second question concerned the processes that led to the ML remain-  
506 ing deep in the northern NEAS in spite of the poleward advection of the  
507 low-salinity waters (Figure 9). The simulations show that convective mixing  
508 deepens the ML in the northern NEAS before the waters of lower salinity  
509 reach this region. This fresher water from the south mixes with the high-  
510 salinity NASHSW to ensure that salinity does not increase in this part of the  
511 NEAS in spite of the evaporation. The deep mixed layer survives in the north-  
512 ern NEAS as the wind stirring and convective overturning generate sufficient  
513 turbulent energy for the ML to maintain the depth attained in January.

514 The third question concerned the SST: why is it almost constant even  
515 though the MLD changes by over 50 m during December–February in the  
516 southern NEAS (Figure 9)? Our simulations show that the atmospheric fluxes  
517 tend to cool the ML, but this cooling is countered by the warming due to  
518 horizontal advection (Figure 11). An important process is downwelling, which  
519 tends to warm the ML, almost cancelling the cooling due to entrainment mix-  
520 ing that continues even as the ML shallows in the southern NEAS (Figure 13).  
521 This balance leads to the formation of a weak barrier layer below the ML in  
522 the southern NEAS (Figure 15), precluding cooling by entrainment.

523 This spatio-temporal difference in the evolution of SST and MLD in the  
524 NEAS implies that the former, which is measurable from space, cannot be  
525 used as a proxy for the latter, for which one has to rely on the sparse and



526 sporadic data available from Argo floats. It is now possible to measure salin-  
527 ity from space, but the variation in salinity in the NEAS is of the order of  
528 0.5 psu, currently beyond the measurement accuracy ( $\sim 2$  psu) of the Aquar-  
529 ius salinity sensor (Anonymous 2014) and of the same order as that of the  
530 SMOS (Soil Moisture and Ocean Salinity) sensor ( $\sim 0.36$  psu; Ratheesh et al  
531 2012; Subrahmanyam et al 2013), ruling out the use of these sensors in this  
532 region until accuracies improve. The spatio-temporal changes in salinity in the  
533 NEAS during winter are much smaller than the changes seen in the northern  
534 Bay of Bengal (Wyrтки 1971; Shetye et al 1991b, 1993, 1996; Chatterjee et al  
535 2012), but the physical processes, including the formation of a barrier layer,  
536 are the same. Even the much weaker salinity gradients in the NEAS play an  
537 important role in determining the MLD in the region.

538 The simulations show that SST and MLD in the NEAS respond but weakly  
539 to the intraseasonal bursts evident in the winds and air-sea radiative and heat  
540 fluxes (Figures 9, 11, and 12). More TKE is needed to sustain the deep MLs  
541 of the NEAS than for the much shallower MLs of the northern Bay of Bengal  
542 (Shetye et al 1991b, 1996). These deeper MLs are less susceptible to the weaker  
543 intraseasonal perturbations in the winds, precluding a strong intraseasonal  
544 response of SST and MLD in the NEAS to the intraseasonal variability in  
545 the fluxes. This relative lack of intraseasonal variability in the SST and MLD  
546 in the NEAS is in striking contrast to what happens in the northern Bay of  
547 Bengal (Premkumar et al 2000; Sengupta et al 2001), where the shallow ML

548 can respond rapidly to perturbations in the winds or air-sea heat and radiative  
549 fluxes.

550 The MLD in the NEAS is determined by an interplay of two very different  
551 physical processes. The convective mixing depends on the winds, radiative  
552 fluxes, SST, air temperature, and specific humidity, all of which are local to  
553 the region. For example, the relative weakness of the winds in the northern  
554 NEAS (Figure 6) can be attributed to the Makran Range that rises to a height  
555 of over 1000 m just north of the southern coast of Pakistan (Figure 1). The  
556 easterly component associated with these winds, however, favours downwelling  
557 and these local winds will therefore accentuate the large-scale downwelling  
558 associated with the WICC. Farther south in the NEAS, the winds blow in  
559 from the flatter terrain of the plains of India and Pakistan (Figure 1); these  
560 northeasterly winds are therefore stronger and lead to a higher latent-heat flux  
561 (Figure 6). The other key process is advection by the WICC, whose seasonal  
562 cycle is not locally forced (as realised by Banse (1984) and Shetye and Sheno  
563 (1988)), but has been shown to be primarily forced remotely from the east  
564 coast of India (McCreary et al 1993; Shankar and Shetye 1997; Shankar et al  
565 2002), with the alongshore winds off southwest India also playing a role (Shetye  
566 et al 2008; Amol et al 2012, 2014). These two processes are not necessarily  
567 correlated, implying the possibility of considerable interannual variability in  
568 the evolution and extent of these deep mixed layers in the NEAS.

569 This role of horizontal advection in determining the spatio-temporal vari-  
570 ability of the MLD in the NEAS during winter has implications for water-mass

571 formation in the region. Two of the high-salinity water masses of the Arabian  
572 Sea, the Persian Gulf Water (PGW) mass and Red Sea Water (RSW) mass  
573 (Rochford 1964; Bower et al 2000; Schott and McCreary 2001), form in semi-  
574 enclosed basins (the Persian Gulf and the Red Sea, respectively), and their  
575 region of formation is therefore limited. By inhibiting the formation of deep  
576 MLs in the southern NEAS, the WICC limits the region of formation of the  
577 ASHSW (Rochford 1964) and NASHSW (Banse and Postel 2009). Hence, even  
578 though these water masses form in the open ocean, their region of formation  
579 is also highly restricted. The poleward WICC also constrains the movement of  
580 the water upwelled off the Oman coast during the previous summer monsoon,  
581 forcing it to spread southward via the central Arabian Sea (Valsala 2009).

582 In conclusion, we have shown that advection by the WICC, and therefore  
583 ocean dynamics at the basin scale, plays a significant role in determining the  
584 MLD, and, by extension, the chlorophyll concentration and ecosystem dynam-  
585 ics, in the NEAS. Our results imply that the conventional approach of aver-  
586 aging over boxes (see Figure 3 for an example of such averaging) for studying  
587 the impact of physics on biogeochemistry can mask important details that are  
588 due to advection because it is the advective component of any budget that is  
589 most affected by the averaging process. Changes in air-sea fluxes, in contrast,  
590 tend to occur over larger spatial scales and are less affected by the averaging.

591 Recent data from high-resolution CTD (Conductivity-Temperature-Depth)  
592 sections across fronts and filaments in the NEAS show considerable variation  
593 in the chlorophyll and pigment concentration across these short-scale features

594 (Vipin et al 2015; Roy et al 2015), which too are a consequence of dynamics.  
595 These data suggest that the response of the ecosystem to the physical forcing  
596 may depend on when the front or filament forms during the winter monsoon,  
597 there being a difference between the fronts that form in November, when the  
598 convective mixing starts to deepen the ML in the NEAS, and the fronts that  
599 form in late January, when the ML reaches its maximum depth (Roy and Anil  
600 2015). Therefore, the seasonal evolution of the ML in the NEAS during the  
601 winter monsoon has an impact even on processes that occur on a much smaller  
602 spatial scale and over a much shorter temporal scale. Our results show that  
603 this variation of the ML in the NEAS, which is a small, but productive, part of  
604 the Arabian Sea, is the result of a more complex interplay of physical processes  
605 than hitherto believed.

606 These results, which highlight the role of advection and salinity in deter-  
607 mining the MLD and SST in the NEAS, have implications for the Indian sum-  
608 mer monsoon as well (Raghu Murtugudde, personal communication, 2015).  
609 Coupled-model studies show that the chlorophyll concentration during late  
610 spring (March) in the northern Arabian Sea has an impact on the model MLD,  
611 which, in turn, has an impact on the summer-monsoon precipitation (Turner  
612 et al 2012). Coupled models also tend to exhibit a cold bias in the SST in  
613 the northern Arabian Sea and this cold bias tends to decrease the summer-  
614 monsoon precipitation (Levine and Turner 2011; Marathayil et al 2013; Levine  
615 et al 2013; Sandeep and Ajayamohan 2014). Our results suggest that it is im-  
616 portant for the coupled models to simulate the salinity correctly because it

---

617 has a significant influence on the spring MLD even though the variations in  
618 SSS in the NEAS are an order of magnitude smaller than in the northern Bay  
619 of Bengal, where the role of the surface low-salinity surface layer in keeping  
620 the bay warmer during the summer monsoon is better documented (see, for  
621 example, Shenoi et al 2002).

622 **Acknowledgements** This study was funded by the OCEAN FINDER programme of  
623 CSIR-NIO. We thank S. R. Shetye for inspiring this programme, K. Banse for pointing  
624 (D. Shankar) to the need for the NEAS to be “looked at by young and fresh minds”,  
625 A. C. Anil for several useful discussions on the ecosystem dynamics of the region, A. Mukher-  
626 jee for his assistance with the model, and Amol Prakash for help with Ferret, which has been  
627 used extensively for analysis and graphics. Comments from Raghu Murtugudde, Theodore  
628 Durland, Dileep Kumar, and Kerala Varma on a preprint and the critical comments of  
629 two anonymous reviewers helped improve the manuscript. The model was run on the high-  
630 performance-computing (HPC) systems at CSIR-CMMACS and CSIR-NIO; the support  
631 provided by Ashalata Marandi and the staff handling these HPC systems is gratefully  
632 acknowledged. R. Remya acknowledges the Council of Scientific and Industrial Research  
633 (CSIR; for financial support) and AcSIR; P. N. Vinayachandran and A. Behera acknowledge  
634 funding from INCOIS under the HOOFS (High-resolution Operational Ocean Forecast and  
635 reanalysis System) programme. This is CSIR-NIO contribution XXXX and ESSO-INCOIS  
636 contribution YYYY.

## 637 **References**

- 638 Adcroft A, Campin JM (2004) Rescaled height coordinates for accurate representation of  
639 free-surface flows in ocean circulation models. *Ocean modelling* 7:269–284
- 640 Amol P, Shankar D, Aparna SG, Shenoj SSC, Fernando V, Mukherjee A, Agarvedekar Y,  
641 Khalap ST, Satelkar NP (2012) Observational evidence from direct current measure-  
642 ments for propagation of remotely forced waves on the shelf off the west coast of India.  
643 *Journal of Geophysical Research* 117, C05017, DOI:10.1029/2011JC007606
- 644 Amol P, Shankar D, Fernando V, Mukherjee A, Aparna SG, Fernandes R, Michael GS,  
645 Khalap ST, Satelkar NP, Agarvedekar Y, Gaonkar MG, Tari AP, Kankonkar A, Vernekar  
646 SP (2014) Observed intraseasonal and seasonal variability of the West India Coastal  
647 Current on the continental slope. *Journal of Earth System Science* 123:1045–1074

- 648 Anonymous (2014) Aquarius User Guide: Aquarius Dataset Version 3.0, Guide Version  
649 6.0, JPL-D-70012, AQ-010-UG-0008. Physical Oceanography Distributed Active Archive  
650 Center (PO.DAAC), Jet Propulsion Laboratory, Pasadena, California, USA
- 651 Antonov JI, Seidov D, Boyer TP, Locarnini RA, Mishonov AV, Garcia HE (2010) World  
652 Ocean Atlas 2009, Volume 2: Salinity. Noaa atlas nesdis 69, NOAA, U. S. Gov. Printing  
653 Office, Washington, D. C.
- 654 Banse K (1968) Hydrography of the Arabian Sea shelf of India and Pakistan and effects on  
655 demersal fishes. *Deep-Sea Research* 15:45–79
- 656 Banse K (1984) Marine geology and oceanography of Arabian Sea and coastal Pakistan.  
657 Van Nostrand Reinhold Co., Scientific and Academic Editions
- 658 Banse K (1987) Seasonality of phytoplankton chlorophyll in the central and northern Ara-  
659 bian Sea. *Deep-Sea Research* 34:713–723
- 660 Banse K, Postel JR (2009) Wintertime convection and ventilation of the upper pycn-  
661 ocline in the northernmost Arabian Sea. *Geophysical Monograph Series* 185:87–117,  
662 DOI:10.1029/2008GM000704
- 663 Bower A, Hunt HD, Price JF (2000) Character and dynamics of the Red Sea and Persian  
664 Gulf outflows. *Journal of Geophysical Research* 105:6387–6414
- 665 Bryan K, Lewis LJ (1979) A water mass model of the world ocean. *Journal of Geophysical*  
666 *Research* 84:2503–2517
- 667 Carruthers JN, Gogate SS, Naidu JR, Laevastu T (1959) Shorewards upslope of the layer  
668 of minimum oxygen off Bombay: it influence on marine biology, particularly fisheries.  
669 *Nature* 183:1084–1087
- 670 Chatterjee A, Shankar D, Shenoi SSC, Reddy GV, Michael GS, Ravichandran M, Gopalkr-  
671 ishna VV, Rao EPR, Bhaskar TVSU, Sanjeevan VN (2012) A new atlas of temperature  
672 and salinity for the North Indian Ocean. *Journal of Earth System Science* 121:559–593,  
673 DOI:10.1007/s12040-012-0191-9
- 674 Chatterjee A, Shankar D, McCreary JP, Vinayachandran PN (2013) Yanai waves in the  
675 western equatorial Indian Ocean. *Journal of Geophysical Research* 118:1556–1570,  
676 DOI:10.1002/jgrc.20121

- 
- 677 Cronin MF, Sprintall J (2001) Wind and buoyancy-forced upper ocean. In: Steele JH,  
678 Turekian KK, Thorpe SA (eds) Encyclopedia of Ocean Science, Academic Press,  
679 DOI:10.1006/rwos.2001.0157
- 680 Gibson JK, Kallberg P, Uppala S, Hernandez A, Serrano ANE (1997) ECMWF Reanalysis  
681 Project Report Series: 1. ERA-15 description. Tech. rep., European Centre for Medium-  
682 Range Weather Forecasting
- 683 Gomes HR, Goes JI, Matondkar SGP, Buskey EJ, basu S, Parab S, Thoppil P (2014) Massive  
684 outbreaks of *Noctiluca scintillans* blooms in the Arabian Sea due to spread of hypoxia.  
685 Nature Communications, DOI:10.1038/ncomms5862
- 686 Griffies SM (2009) Elements of MOM4p1. GFDL Ocean Group Tech. Rep. 6,  
687 NOAA/Geophysical Fluid Dynamics Laboratory, Available online at  
688 <http://www.gfdl.noaa.gov/>
- 689 Griffies SM, Hallberg RW (2000) Biharmonic friction with a Smagorinsky viscosity for use  
690 in large-scale eddy-permitting ocean models. Monthly Weather Review 128:2935–2946
- 691 Han W (1999) Influence of salinity on dynamics, thermodynamics and mixed-layer physics  
692 in the Indian Ocean. PhD thesis, Nova Southeastern University
- 693 Han W, McCreary JP, Kohler KE (2001) Influence of precipitation minus evaporation and  
694 Bay of Bengal rivers on dynamics, thermodynamics, and mixed layer physics in the  
695 upper Indian Ocean. Journal of Geophysical Research 106:6895–6916
- 696 Hood RR, Wiggert JD, Naqvi SWA (2009) Indian Ocean Research: Opportunities and Chal-  
697 lenges. Geophysical Monograph Series 185:409–428, DOI:10.1029/2008GM000714
- 698 Jackett DR, McDougall TJ, Feistel R, Wright DG, Griffies SM (2006) Algorithms for density,  
699 potential temperature, conservative temperature, and freezing temperature of seawater.  
700 Journal of Atmospheric and Oceanic Technology 23:1709–1728
- 701 Koné V, Aumont O, Lévy M, Resplandy L (2009) Physical and biogeochemical controls of  
702 the phytoplankton seasonal cycle in the Indian Ocean: A modeling study. Geophysical  
703 Monograph Series 185:147–166, DOI:10.1029/2008GM000700
- 704 Kraus EB, Turner JS (1967) A one-dimensional model of the seasonal thermocline. II: The  
705 general theory and its consequences. Tellus 119:98–106



- 706 Kurian J, Vinayachandran PN (2007) Mechanisms of formation of Arabian Sea mini  
707 warm pool in a high-resolution OGCM. *Journal of Geophysical Research* 112,  
708 DOI:10.1029/2006JC003631, C05009
- 709 Large WG, McWilliams JC, Doney SC (1994) Oceanic vertical mixing: a review and a model  
710 with a nonlocal boundary layer parameterization. *Reviews of Geophysics* 32:363–403
- 711 Levine RC, Turner AG (2011) Dependence of Indian monsoon rainfall on moisture fluxes  
712 across the Arabian Sea and the impact of coupled model sea surface temperature biases.  
713 *Climate Dynamics* 38:2167–2190, DOI:10.1007/s00382-011-1096-z
- 714 Levine RC, Turner AG, Marathayil D, Martin GM (2013) The role of northern Arabian  
715 Sea surface temperature biases in CMIP5 model simulations and future projections of  
716 Indian summer monsoon rainfall. *Climate Dynamics* 41:155–172, DOI:10.1007/s00382-  
717 012-1656-x
- 718 Levitus S (1982) *Climatological atlas of the world ocean*. NOAA Professional Paper 13, 173  
719 pp., U.S. Government Printing Office, Washington D.C.
- 720 Lévy M, Andre JM, Shankar D, Durand F, Shenoi SSC (2006) A quantitative method for  
721 describing the seasonal cycles of surface chlorophyll in the Indian Ocean. In: Frouin  
722 RJ, Agarwal VK, Kawamura H, Nayak S, Pan D (eds) *Remote sensing of the marine  
723 environment*, Proceedings of SPIE, vol 6406
- 724 Lévy M, Shankar D, Andre JM, Shenoi SSC, Durand F, Montégut CD (2007) Basin-wide  
725 seasonal evolution of the Indian Ocean’s phytoplankton blooms. *Journal of Geophysical  
726 Research* 112, DOI:10.1029/2007JC004090, C12014
- 727 Locarnini RA, Mishonov AV, Antonov JI, Boyer TP, Garcia HE (2010) *World Ocean Atlas  
728 2009, Volume 1: Temperature*. Noaa atlas nesdis 68, NOAA, U. S. Gov. Printing Office,  
729 Washington, D. C.
- 730 Lukas RB, Lindström EJ (1991) The mixed layer of the western equatorial Pacific Ocean.  
731 *Journal of Geophysical Research* 96:3343–3357
- 732 Madhupratap M, Prasannakumar S, Bhattathiri PMA, Raghukumar S, Nair KKC, Ramaiah  
733 N (1996) Mechanism of biological response to winter cooling in the northeastern Arabian  
734 Sea. *Nature* 384:549–552

- 735 Marathayil D, Turner AG, Shaffrey LC, Levine RC (2013) Systematic winter sea-surface  
736 temperature biases in the northern Arabian Sea in HiGEM and the CMIP3 models.  
737 *Environmental Research Letters* 8, DOI:10.1088/1748-9326/8/1/014028, 014028
- 738 Mariano AJ, Ryan EH, Perkins BD, Smithers S (1995) The Mariano global surface velocity  
739 analysis 1.0. Tech. Rep. USCG Report CG-D-34-95, USCG
- 740 McCreary JP, Kundu PK, Molinary RL (1993) A numerical investigation of the dynamics,  
741 thermodynamics and mixed layer processes in the Indian Ocean. *Progress in Oceanog-*  
742 *raphy* 31:181–224
- 743 McCreary JP, Kohler KE, Hood RR, Olson DB (1996) A four-component ecosystem  
744 model of biological activity in the Arabian Sea. *Progress in Oceanography* 37:193–240,  
745 DOI:S0079-6611(96)00005-5
- 746 McCreary JP, Kohler KE, Hood RR, Smith S, Kindle J, Fischer AS, Weller RA (2001)  
747 Influences of diurnal and intraseasonal forcing on mixed-layer and biological variability  
748 in the central Arabian Sea. *Journal of Geophysical Research* 106:7139–7155
- 749 McCreary JP, Murtugudde R, Vialard J, Vinayachandran PN, Wiggert JD, Hood RR,  
750 Shankar D, Shetye S (2009) Biophysical Processes in the Indian Ocean. *Geophysical*  
751 *Monograph Series* 185:9–32, DOI:10.1029/2008GM000768
- 752 Monin AS, Obukhov AM (1954) Basic laws of turbulent mixing in the surface layer of the  
753 atmosphere. *Trudy Geofizicheskogo Instituta, Akademiya Nauk SSSR* 24:163–187
- 754 Morel A, Antoine D (1994) Heating rate within the upper ocean in relation to its biooptical  
755 state. *Journal of Physical Oceanography* 24:1652–1665
- 756 Naqvi SWA (1991) Geographical extent of denitrification in the Arabian Sea in relation to  
757 some physical processes. *Oceanologica Acta* 14:281–290
- 758 Naqvi SWA, Narvekar PV, Desa E (2006) Coastal biogeochemical processes in the north  
759 Indian Ocean. Coastal segment (14,S–W). In: Robinson AR, Brink KH (eds) *The Sea*,  
760 vol 14, John Wiley and Sons, Inc, chap 19, pp 723–781
- 761 Pankajakshan T, Ramaraju DV (1987) Intrusion of bay of bengal water into the arabian  
762 sea along the west coast of india during northeast monsoon. In: Rao TSS, Natarajan  
763 R, Desai BN, Swami GN, Bhat SR (eds) *Contributions in marine sciences*. Dr. S. Z.

- 764 Quasim Sastyabdapurthi felicitation volume, National Institute of Oceanography, Dona  
765 Paula, Goa, India, pp 237–244
- 766 Papa F, Durand F, Rossow WB, Rahman A, Bala S (2010) Satellite altimeter-  
767 derived monthly discharge of the Ganga-Brahmaputra river and its seasonal to  
768 interannual variations from 1993 to 2008. *Journal of Geophysical Research* 115,  
769 DOI:10.1029/2009JC006075, C12013
- 770 Prasad TG, Ikeda M (2002a) A numerical study of the seasonal variability of Arabian Sea  
771 high-salinity water. *Journal of Geophysical Research* 107, DOI:10.1029/2001JC001139,  
772 3197
- 773 Prasad TG, Ikeda M (2002b) The wintertime water mass formation in the northern Arabian  
774 Sea: A model study. *Journal of Physical Oceanography* 32:1028–1040
- 775 Prasannakumar S, Prasad TG (1996) Winter cooling in the northern Arabian Sea. *Current*  
776 *Science* 71:834–841
- 777 Prasannakumar S, Prasad TG (1999) Formation and spreading of Arabian Sea high-salinity  
778 water mass. *Journal of Geophysical Research* 104:1455–1464
- 779 Praveenkumar B, Vialard J, Lengaigne M, Murty VSN, McPhaden MJ (2012) TropFlux: air-  
780 sea fluxes for the global tropical oceans — description and evaluation. *Climate Dynamics*  
781 38:1521–1543, DOI:10.1007/s00382-011-1115-0
- 782 Premkumar K, Ravichandran M, Kalsi SR, Sengupta D, Gadgil S (2000) First results from  
783 a new observational system over the Indian seas. *Current Science* 78:323–331
- 784 Qiu B, Kelly KA (1993) Upper-ocean heat balance in the Kuroshio extension region. *Journal*  
785 *of Physical Oceanography* 23:2027–2041
- 786 Rao SA, Gopalakrishna VV, Shetye SR, Yamagata T (2002) Why were cool SST anomalies  
787 absent in the Bay of Bengal during the 1997 Indian Ocean Dipole event? *Geophysical*  
788 *Research Letters* 29, DOI:10.1029/2001GL014645, 1555
- 789 Ratheesh S, Mankad B, Basu S, Kumar R, Sharma R (2012) Assessment of satellite-derived  
790 sea-surface salinity in the Indian Ocean. *IEEE Geoscience and Remote Sensing Letters*  
791 10:428–431, DOI:10.1109/LGRS.2012.2207943

- 792 Rochford DJ (1964) Salinity maxima in the upper 1000 m of the north Indian Ocean.  
793 Australian Journal of Marine and Freshwater Research 15:1–24
- 794 Röske F (2001) An atlas of surface fluxes based on the ECMWF Reanalysis — A climato-  
795 logical data set to force global ocean general circulation models. Tech. Rep. Tech. Rep.  
796 323, Max-Planck Institut für Meteorologie, Hamburg, Germany
- 797 Roy R, Anil AC (2015) Complex interplay of physical forcing and *Prochlorococcus* population  
798 in ocean. Progress in Oceanography (in press), DOI:10.1016/j.pocean.2015.06.010
- 799 Roy R, Chithari R, Kulkarni V, Krishna MS, Sarma VVSS, Anil AC (2015)  
800 CHEMTAX-derived phytoplankton community structure associated with tempera-  
801 ture fronts in the northeastern Arabian Sea. Journal of Marine Systems 144:81–91,  
802 DOI:10.1016/j.jmarsys.2014.11.009
- 803 Sandeep S, Ajayamohan RS (2014) Origin of cold bias over the Arabian Sea in climate  
804 models. Scientific Reports 4, DOI:10.1038/srep06403
- 805 Schott FA, McCreary JP (2001) The monsoon circulation of the Indian Ocean. Progress in  
806 Oceanography 51:1–123
- 807 Sengupta D, Goswami BN, Senan R (2001) Coherent intraseasonal oscillation of ocean and  
808 atmosphere during the Asian summer monsoon. Geophysical Research Letters 28:4127–  
809 4130
- 810 Shankar D (1998) Low-frequency variability of sea level along the coast of India. PhD thesis,  
811 Goa University, Goa, India
- 812 Shankar D (2000) Seasonal cycle of sea level and currents along the coast of India. Current  
813 Science 78:279–288
- 814 Shankar D, Shetye SR (1997) On the dynamics of the Lakshadweep high and low in the  
815 southeastern Arabian Sea. Journal of Geophysical Research 102:12,551–12,562
- 816 Shankar D, Vinayachandran P, Unnikrishnan AS (2002) The monsoon currents in the north  
817 Indian Ocean. Progress in Oceanography 52:63–120
- 818 Shankar D, Gopalakrishna VV, Shenoi SSC, Durand F, Shetye SR, Rajan CK, Johnson Z,  
819 Araligidad N, Michael GS (2004) Observational evidence for westward propagation of  
820 temperature inversions in the southeastern Arabian Sea. Geophysical Research Letters

- 821 31, DOI:10.1029/2004GL019652, L08305
- 822 Shankar D, Aparna SG, McCreary JP, Suresh I, Neetu S, Durand F, Shenoi SSC, Saafani  
823 MAA (2010) Minima of interannual sea-level variability in the Indian Ocean. *Progress*  
824 *in Oceanography* 84(3–4):225–241, DOI:10.1016/j.pocean.2009.10.002
- 825 Sharma GS (1968) Seasonal variation of some hydrographic properties of the shelf waters off  
826 the west coast of India. *Bulletin of the National Institute of Science of India* 38:263–276
- 827 Shenoi SSC, Shetye SR, Gouveia AD, Michael GS (1993) Salinity extrema in the Arabian  
828 Sea. In: Ittekkot V, Nair RR (eds) *Monsoon biogeochemistry*, *Mitteilungen aus dem*  
829 *Geologisch-Paläontologischen Institut der Universität Hamburg*, vol 76, SCOPE/UNEP  
830 *Sonderband*, pp 37–49
- 831 Shenoi SSC, Shankar D, Shetye SR (2002) Differences in heat budgets of the near-surface  
832 Arabian Sea and Bay of Bengal: Implications for the summer monsoon. *Journal of*  
833 *Geophysical Research* 107, DOI:10.1029/2000JC000679
- 834 Shenoi SSC, Shankar D, Shetye SR (2004) Remote forcing annihilates barrier layer in south-  
835 eastern Arabian Sea. *Geophysical Research Letters* DOI:10.1029/2003GL019270, L05307
- 836 Shetye SR, Almeida AM (1985) An examination of the factors that influence the monthly-  
837 mean sea level along the coast of India. In: *IOC/Unesco Workshop on Regional Co-*  
838 *operation in Marine Science in the Central Indian Ocean and Adjacent Seas and Gulfs*,  
839 *Colombo, Sri Lanka, IOC Workshop Reports*, vol 37, pp 87–104
- 840 Shetye SR, Gouveia AD (1998) Coastal circulation in the north Indian Ocean. *Coastal*  
841 *segment (14,S–W)*. In: Robinson AR, Brink KH (eds) *The Sea*, vol 11, John Wiley and  
842 *Sons, Inc*, chap 18, pp 523–556
- 843 Shetye SR, Shenoi SSC (1988) Seasonal cycle of surface circulation in the coastal north  
844 Indian Ocean. *Proceedings of the Indian Academy of Sciences (Earth and Planetary*  
845 *Sciences)* 97:53–62
- 846 Shetye SR, Gouveia AD, Shenoi SSC, Sundar D, Michael GS, Almeida AM, Santanam K  
847 (1990) Hydrography and circulation off the west coast of India during the southwest  
848 monsoon 1987. *Journal of Marine Research* 48:359–378

- 
- 849 Shetye SR, Gouveia AD, Shenoi SSC, Michael GS, Sundar D, Almeida AM, Santanam K  
850 (1991a) The coastal current off western India during the northeast monsoon. *Deep-Sea*  
851 *Research* 38:1517–1529
- 852 Shetye SR, Shenoi SSC, Gouveia AD, Michael GS, Sundar D, Nampoothiri G (1991b) Wind-  
853 driven coastal upwelling along the western boundary of the Bay of Bengal during the  
854 southwest monsoon. *Continental Shelf Research* 11:1397–1408
- 855 Shetye SR, Gouveia AD, Shenoi SSC (1992) Does winter cooling lead to the subsurface  
856 salinity minimum off Saurashtra, India. In: Desai BN (ed) *Oceanography of the Indian*  
857 *Ocean*, Oxford and India Book House, pp 617–625
- 858 Shetye SR, Gouveia AD, Shenoi SSC, Sundar D, Michael GS, Nampoothiri G (1993) The  
859 western boundary current of the seasonal subtropical gyre in the Bay of Bengal. *Journal*  
860 *of Geophysical Research* 98:945–954
- 861 Shetye SR, Gouveia AD, Shankar D, Shenoi SSC, Vinayachandran PN, Sundar D, Michael  
862 GS, Nampoothiri G (1996) Hydrography and circulation in the western Bay of Bengal  
863 during the northeast monsoon. *Journal of Geophysical Research* 101:14,011–14,025
- 864 Shetye SR, Suresh I, Shankar D, Sundar D, Jayakumar S, Mehra P, Prabhudesai RG, Ped-  
865 nekar PS (2008) Observational evidence for remote forcing of the West India Coastal  
866 Current. *Journal of Geophysical Research* 113, C11001, DOI:10.1029/2008JC004874
- 867 Sindhu B, Suresh I, Unnikrishnan AS, Bhatkar NV, Neetu S, Michael GS (2007) Improved  
868 bathymetric datasets for the shallow water regions in the Indian Ocean. *Journal of Earth*  
869 *System Science* 116:261–274
- 870 Stacey MW, Pond S, Nowak ZP (1995) A numerical model of the circulation in Knight Inlet,  
871 British Columbia, Canada. *Journal of Physical Oceanography* 25:1037–1062
- 872 Subrahmanyam B, Grunseich G, Nyadjro ES (2013) Preliminary SMOS salinity measure-  
873 ments and validation in the Indian Ocean. *IEEE Transactions on Geoscience and Remote*  
874 *Sensing* 51:19–27, DOI:10.1109/TGRS.2012.2199122
- 875 Sweeney C, Gnanadesikan A, Griffies SM, Harrison MJ, Rosati AJ, Samuels BL (2005) Im-  
876 pacts of shortwave penetration depth on large-scale ocean circulation and heat transport.  
877 *Journal of Physical Oceanography* 35:1103–1119, DOI:10.1175/JPO2740.1

- 878 Turner AG, Joshi M, Robertson ES, Woolnough SJ (2012) The effect of Arabian Sea optical  
879 properties on SST biases and the South Asian summer monsoon in a coupled GCM.  
880 *Climate Dynamics* 39:811–826, DOI:10.1007/s00382-011-1254-3
- 881 Valsala V (2009) Different spreading of Somali and Arabian coastal upwelled waters in the  
882 northern Indian Ocean: A case study. *Journal of Oceanography* 65:803–816
- 883 Varma KK, Das VK, Gouveia AD (1980) Thermohaline structure and watermasses in the  
884 northern Arabian Sea during February–April. *Indian Journal of Marine Sciences* 9:148–  
885 155
- 886 Vialard J, Delecluse P (1998) An OGCM study for the TOGA decade. Part II: Barrier-layer  
887 formation and variability. *Journal of Physical Oceanography* 28:1089–1106
- 888 Vinayachandran PN, Kurian J, Neema CP (2007) Indian Ocean response to anomalous  
889 conditions during 2006. *Geophysical Research Letters* 34, DOI:10.1029/2007GL030194
- 890 Vipin P, Sarkar K, Aparna SG, Shankar D, Sarma VVSS, Gracias DG, Krishna MS, Srikanth  
891 G, Mandal R, Rao EPR, Rao NS (2015) Evolution and sub-surface characteristics of an  
892 SST filament and front in the northeastern Arabian Sea during November–December  
893 2012. *Journal of Marine Systems* 150, DOI:10.1016/j.jmarsys.2015.05.003
- 894 Vörösmarty CJ, Fekete B, Tucker BA (1996) River Discharge Database, Version 1.0 (RivDIS  
895 v1.0), vols. 0–6, A contribution to IHP-V Theme 1, Technical Documents in Hydrology  
896 Series. Technical report, UNESCO, Paris
- 897 Wiggert JD, Jones BH, Hickey TD, Weller RA, Brink KH, Marra J, Codispoti LA (2000)  
898 The northeast monsoon’s impact on mixing, phytoplankton biomass and nutrient cycling  
899 in the Arabian Sea. *Deep-Sea Research, Part II* 47:1353–1385
- 900 Wiggert JD, Murtugudde RG, McClain CR (2002) Processes controlling interannual varia-  
901 tions in wintertime (northeast monsoon) biomass in the central Arabian Sea. *Deep-Sea*  
902 *Research, Part II* 49:2319–2343
- 903 Wiggert JD, Hood RR, Banse K, Kindle JC (2005) Monsoon-driven biogeochemical processes  
904 in the Arabian Sea. *Progress in Oceanography* 65:176–213
- 905 Wiggert JD, Murtugudde RG, Christian JR (2006) Annual ecosystem variability in the  
906 tropical Indian Ocean: Results of a coupled bio-physical ocean general circulation model.

- 
- 907        Deep-Sea Research, Part II 53:644–676
- 908        Wiggert JD, Vialard J, Behrenfeld MJ (2009) Basin-wide modification of dynamical and  
909        biogeochemical processes by the positive phase of the Indian Ocean dipole during the  
910        SeaWiFS era. *Geophysical Monograph Series* 185:385–407, DOI:10.1029/2008GM000776
- 911        Wyrтки K (1971) *Oceanographic Atlas of the International Indian Ocean Expedition*. Na-  
912        tional Science Foundation, Washington, D.C., 531 pp.
- 913        Xie P, Arkin PA (1997) Global precipitation: A 17-year monthly analysis based on gauge  
914        observations, satellite estimates, and numerical model outputs. *Bullitein of American*  
915        *Meteorological Soceity* 78:2539–2558

916        **Tables**



Physics	Remarks	Reference / source
Coordinate system	Generalised orthogonal coordinates horizontally and quasi-horizontal, rescaled height coordinate vertically	Stacey et al (1995) Adcroft and Campin (2004)
Bottom topography	Modified ETOPO2 bathymetry	Sindhu et al (2007)
Initial temperature and salinity fields (also used for relaxation at open boundaries)	Adds data from the Indian EEZ (Exclusive Economic Zone) to the World Ocean Atlas of Locarnini et al (2010) and Antonov et al (2010)	Chatterjee et al (2012)
Equation of state	Nonlinear formulation	Jackett et al (2006)
Tracer advection	Multi-dimensional, piecewise parabolic method (MDPPM)	<a href="http://mitgcm.org/">http://mitgcm.org/</a>
Vertical mixing	$K$ -profile parameterisation, with a pre-specified vertical-diffusivity profile (Bryan and Lewis 1979) and a critical bulk Richardson number of 0.3 (local mixing due to double diffusion not included to avoid enhanced mixing within the stratified water column)	Large et al (1994)
Horizontal friction	Combination of biharmonic and Laplacian mixing, with Smagorinsky mixing coefficients of 0.01 (velocity scale $0.04 \text{ m s}^{-1}$ ) and 0.1 (velocity scale $0.005 \text{ m s}^{-1}$ ), respectively	Griffies and Hallberg (2000)
Penetrative shortwave heating	In upper 100 m, calculated using a Chl- <i>a</i> based scheme	Morel and Antoine (1994)

**Table 1** Model physics, including coordinate systems and parameterisations used.

Field (units)	Data source	Frequency	Reference
Wind stress ( $\text{N m}^{-2}$ )	OMIP	Daily	Röske (2001)
Wind speed ( $\text{m s}^{-1}$ )	OMIP	Daily	Röske (2001)
Downward shortwave radiation ( $\text{W m}^{-2}$ )	OMIP	Daily	Röske (2001)
Downward longwave radiation ( $\text{W m}^{-2}$ )	OMIP	Daily	Röske (2001)
Air temperature (K)	OMIP	Daily	Röske (2001)
Specific humidity ( $\text{kg kg}^{-1}$ )	OMIP	Daily	Röske (2001)
Precipitation ( $\text{m s}^{-1}$ )	CMAP	Daily	Xie and Arkin (1997)
River runoff ( $\text{m s}^{-1}$ )	SAGE (UNESCO)	Monthly	Vörösmarty et al (1996) Papa et al (2010)
Chlorophyll ( $\text{mg m}^{-3}$ )	SeaWiFS	Monthly	Sweeney et al (2005)

**Table 2** List of data sets used to force the MOM4p1 model. From left to right, the table columns list the data type, source, frequency, and a reference that describes the data.

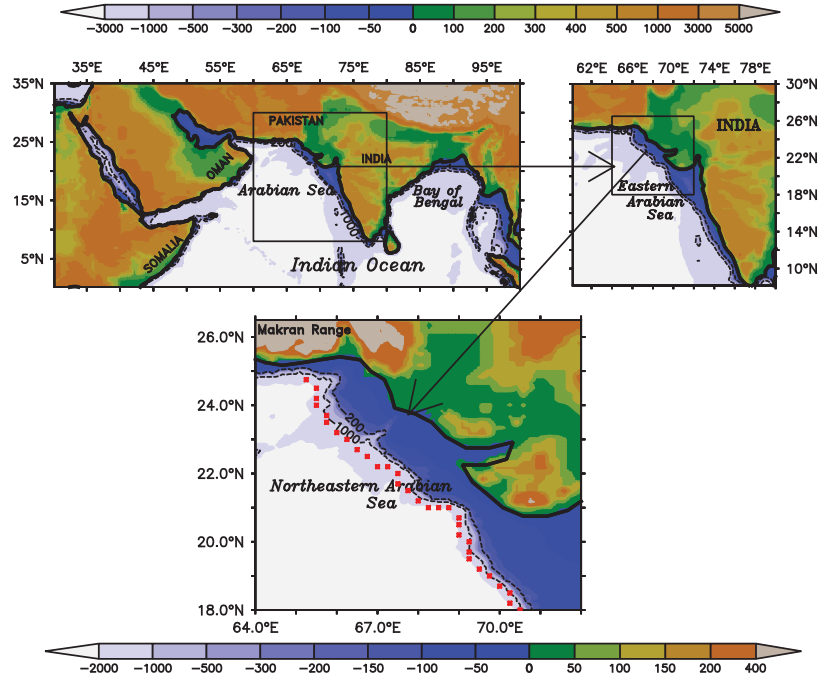


**Fig. 1** Map showing the region of interest. Ocean bathymetry (metres) and land topography (metres) are shown in all three panels. The shelf break is denoted by the 200 m isobath. Several figures in this paper show the variation in the NEAS along the 1000 m isobath, which is also shown; the model grid cells used for these figures are marked by filled red squares. The top left panel shows the large-scale map of the region of the region; the Arabian Sea is the western arm of the north Indian Ocean (NIO). The box marks the eastern Arabian Sea (EAS), which is shown in the top right panel. The topography in these two panels is based on the ETOPO20 data set. The box in the top right panel marks the northeastern Arabian Sea (NEAS), for which most of the spatial maps are plotted; the NEAS is shown in the bottom panel, which is based on the ETOPO5 data set as modified by Sindhu et al (2007).

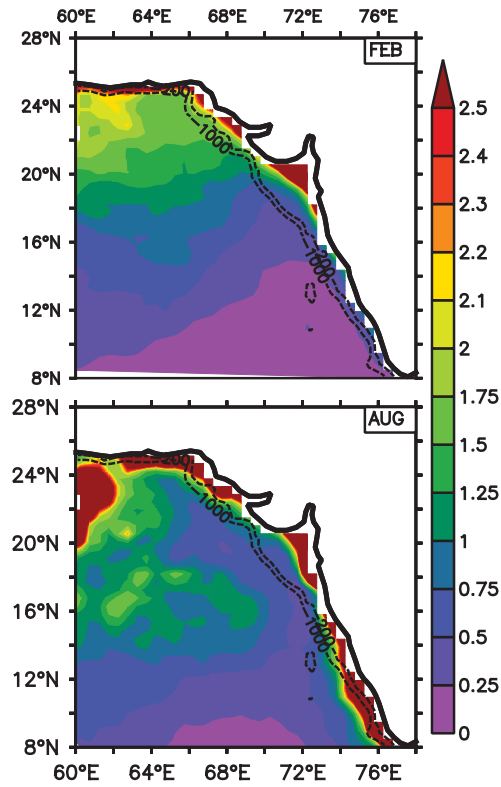


**Fig. 2** Climatological chlorophyll concentration ( $\text{mg m}^{-3}$ ) in the EAS during February (top) and August (bottom); the data are from Lévy et al (2006). Note that the colour scale is not uniform. There is no bloom in the southern EAS during February. The 200 m and 1000 m isobaths are marked.

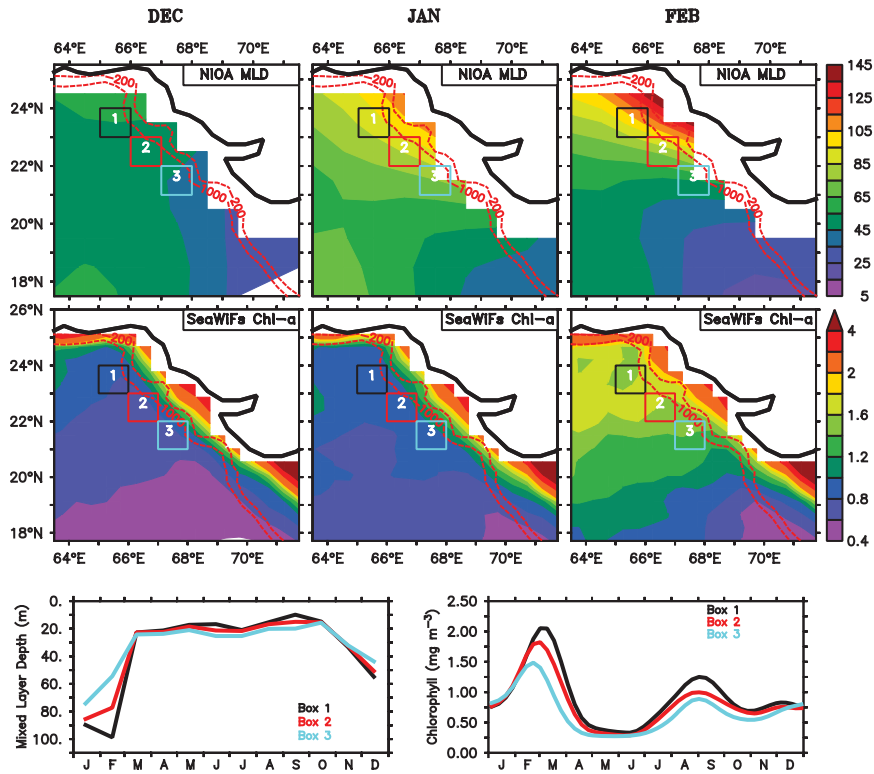


**Fig. 3** Observed monthly climatologies of MLD (metres; top panels), based on the monthly temperature and salinity climatologies of Chatterjee et al (2012) (NIOA: North Indian Ocean Atlas), and chlorophyll concentration ( $\text{mg m}^{-3}$ ; middle panels), based on the weekly climatology of Lévy et al (2006), in the NEAS during December–February (left to right). Note that the colour scale for chlorophyll is not uniform. The 200 m and 1000 m isobaths are marked. The two panels in the bottom row show the annual cycle of MLD (left) and chlorophyll concentration (right) for the three boxes marked in the contour maps. Both MLD and chlorophyll concentration increase from south to north during the winter monsoon (November–February).

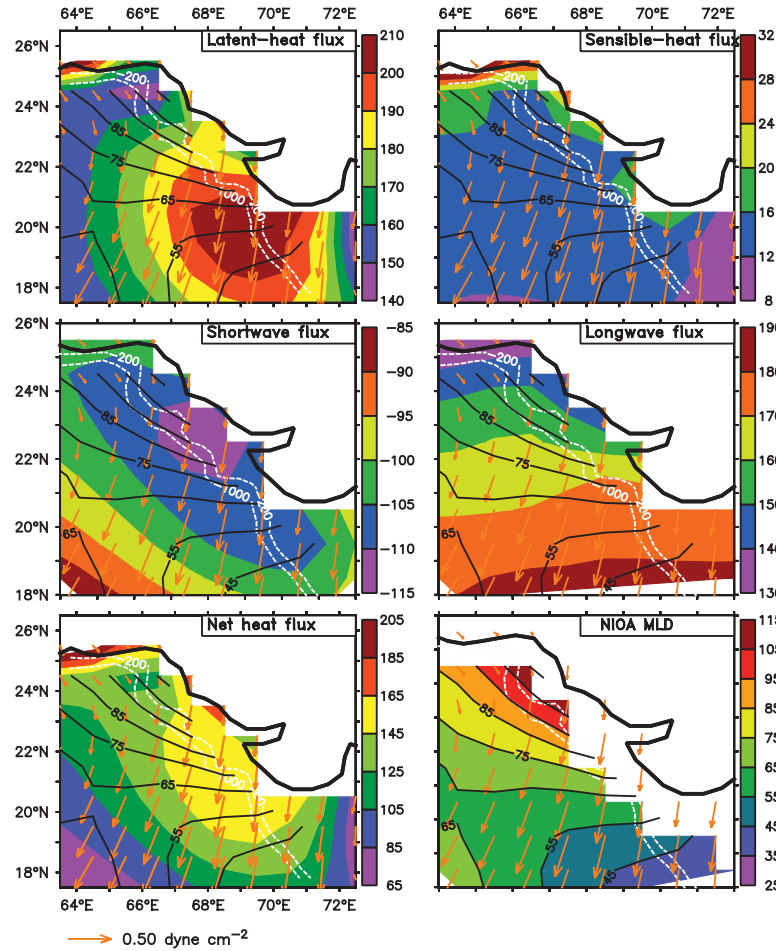


**Fig. 4** Climatological monthly latent heat flux (top left), sensible heat flux (top right), net shortwave flux (middle left), net longwave flux (middle right), and net heat flux (bottom left) during January in the NEAS. Superimposed on these five maps are the MLD contours (metres) for January; the MLD for January is plotted in the bottom right panel. All the fluxes are in  $\text{W m}^{-2}$ , with positive values implying a flux out of the ocean; note that the colour scale is different for each panel. The flux climatologies were computed using data for 1979–2013. Superimposed on the flux and MLD maps are the wind-stress vectors ( $\text{dyne cm}^{-2}$ ). The wind stress and fluxes are from Praveenkumar et al (2012) and the MLD is based on Chatterjee et al (2012). The 200 m and 1000 m isobaths are marked.

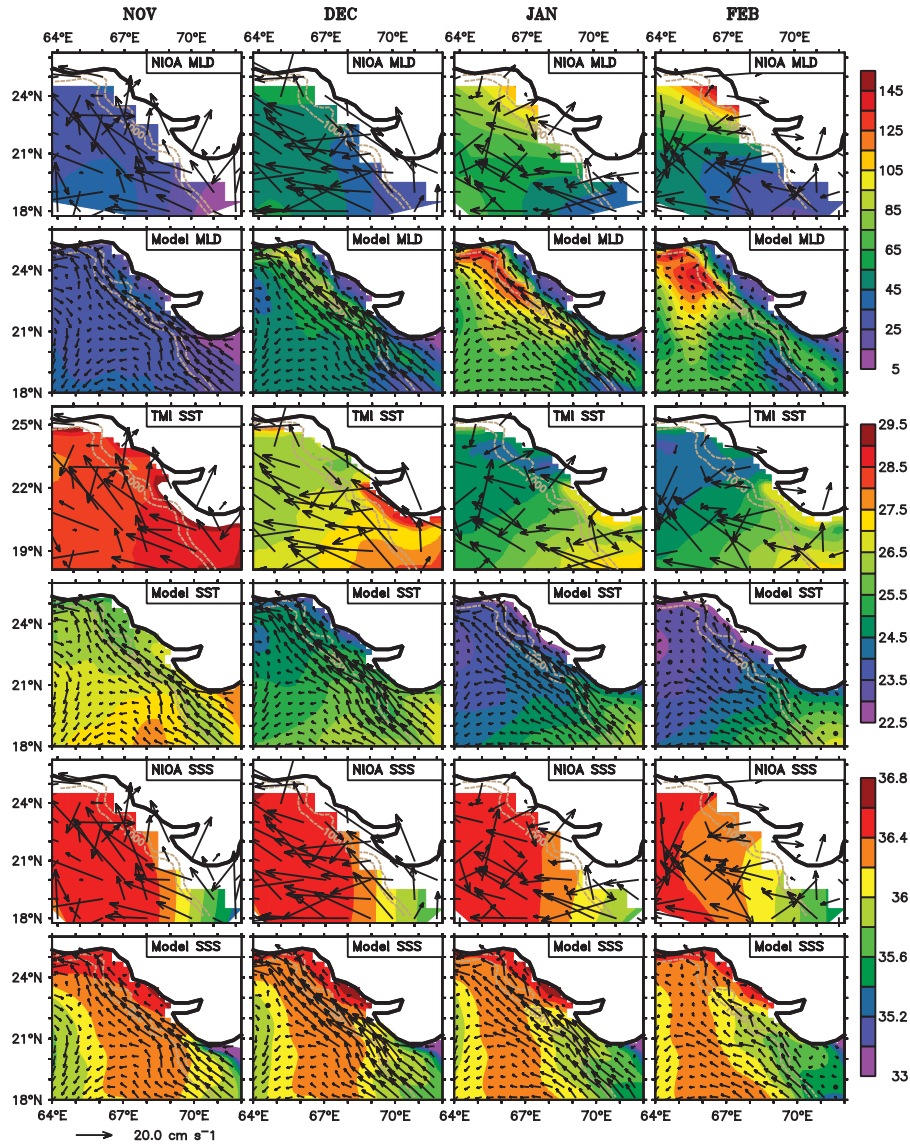


**Fig. 5** Monthly climatologies of observed MLD (first row), model MLD (second row), observed SST (third row), model SST (fourth row), observed SSS (fifth row), and model SSS (sixth row) during November–February (from left to right) for the NEAS. The units are metres for MLD, °C for SST, and psu (practical salinity unit) for SSS. The SST climatology is based on TMI data for 2000–2008 ([ftp://ftp.ssmi.com/tmi/bmaps\\_v04/](ftp://ftp.ssmi.com/tmi/bmaps_v04/)) and the SSS and MLD climatologies are based on Chatterjee et al (2012). Overlaid on all panels are the surface currents ( $\text{cm s}^{-1}$ ). The observed currents, overlaid in the observation panels, are from Mariano et al (1995); the model surface currents are overlaid in the model panels. The 200 m and 1000 m isobaths are marked.

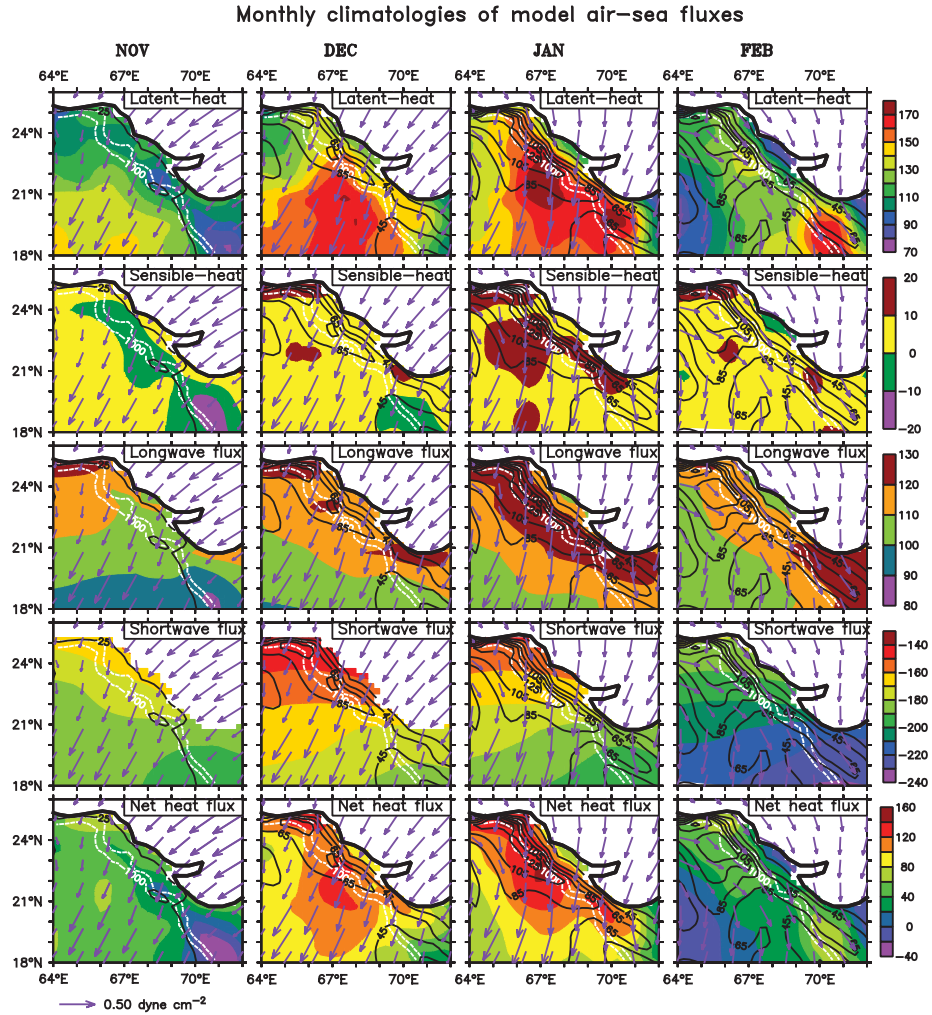


**Fig. 6** Monthly climatologies of the model air-sea flux fields. The daily model fluxes were averaged over the month to obtain these monthly climatologies and the sign convention is that a positive value indicates flux out of the ocean. The variables plotted for November–February (from left to right) are latent-heat flux (first row), sensible-heat flux (second row), net longwave flux (third row), net shortwave flux (fourth row), and net heat flux (fifth row). The model MLD and OMIP wind-stress vectors are superimposed on all the maps; the contour interval for MLD is 20 m. The units are  $\text{W m}^{-2}$  for the fluxes, metres for MLD, and  $\text{dyne cm}^{-2}$  for the wind stress. The 200 m and 1000 m isobaths are marked.



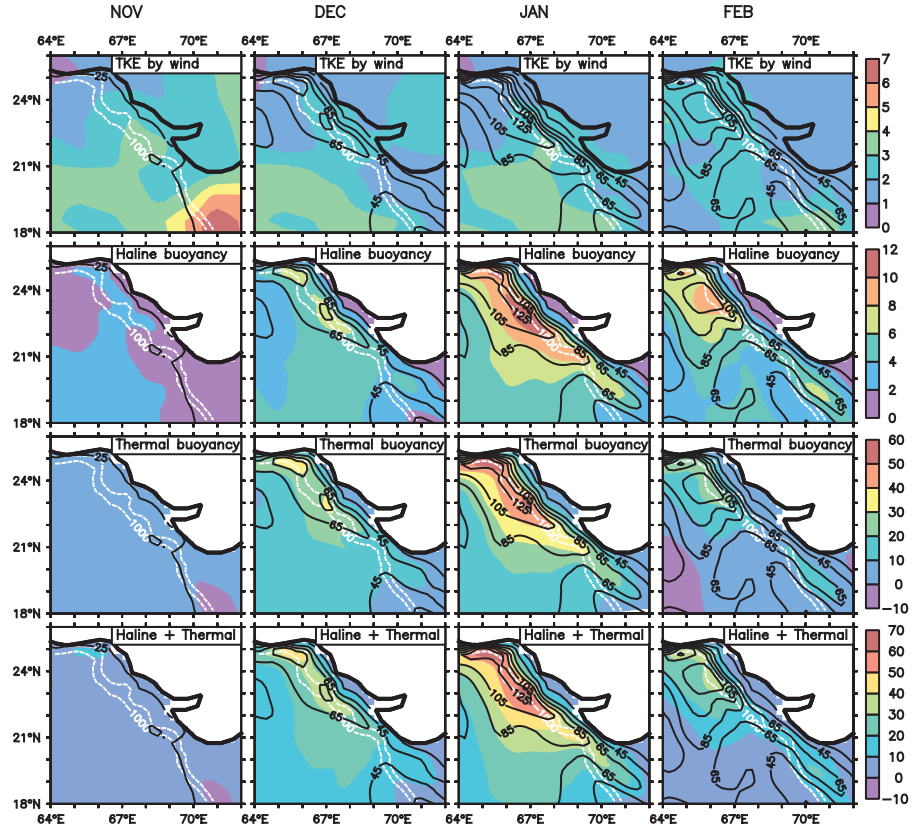


**Fig. 7** Monthly climatologies of the model turbulent kinetic energy due to the wind (first row), haline buoyancy flux (second row), thermal buoyancy flux (third row), and the total buoyancy flux (sum of haline and thermal buoyancy fluxes; fourth row) during November–February (from left to right). All these fields have units of  $10^{-7} \text{ m}^3 \text{ s}^{-3}$  (the values have been multiplied by  $10^7$  before plotting). The daily buoyancy flux was averaged over the month to obtain the monthly climatology. Note that a positive buoyancy flux supports convective mixing and is therefore associated with a net heat flux out of the ocean (for thermal buoyancy flux) and an excess of evaporation over precipitation (for haline buoyancy flux). Overlaid on all panels is the MLD (m); the contour interval for MLD is 20 m. The 200 m and 1000 m isobaths are marked.

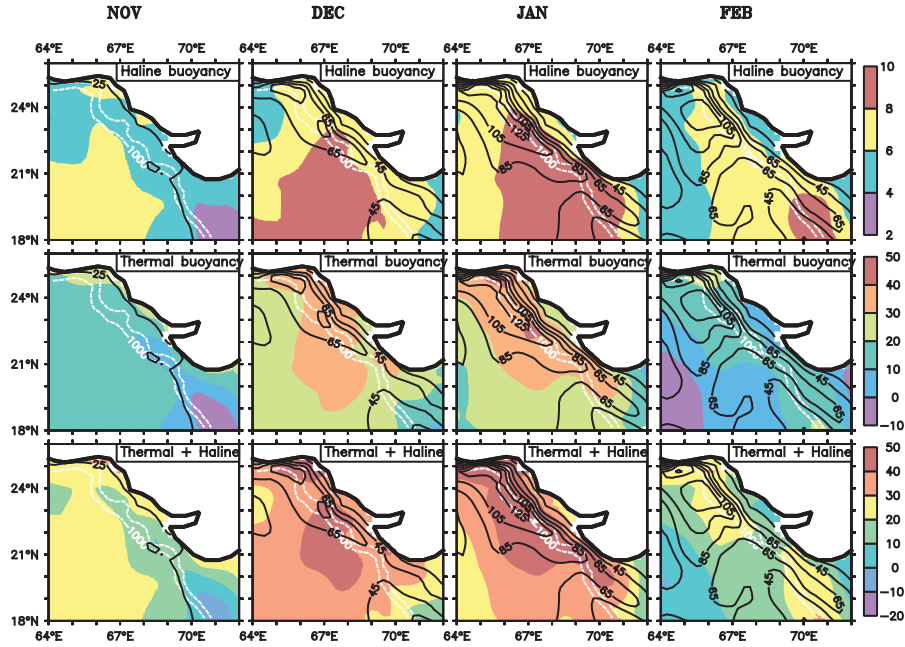


**Fig. 8** Monthly climatologies of the model depth-averaged buoyancy fluxes ( $10^{-9} \text{ m}^2 \text{ s}^{-3}$ ; all values have been multiplied by  $10^9$  before plotting). Haline buoyancy flux (top row), depth-averaged thermal buoyancy flux (middle row), and the sum of these two depth-averaged buoyancy fluxes (bottom row) are shown for November–February (from left to right). The daily buoyancy flux was averaged over the month to obtain the monthly climatology. Overlaid on all panels is the MLD (m); the contour interval for MLD is 20 m. Note the striking difference between the patterns of these depth-averaged buoyancy fluxes and the buoyancy fluxes shown in Figure 7: the depth-averaged fluxes change over a broader region, reflecting the larger scale associated with the changes due to the march of the season, and their pattern does not match that of the MLD. The 200 m and 1000 m isobaths are marked.

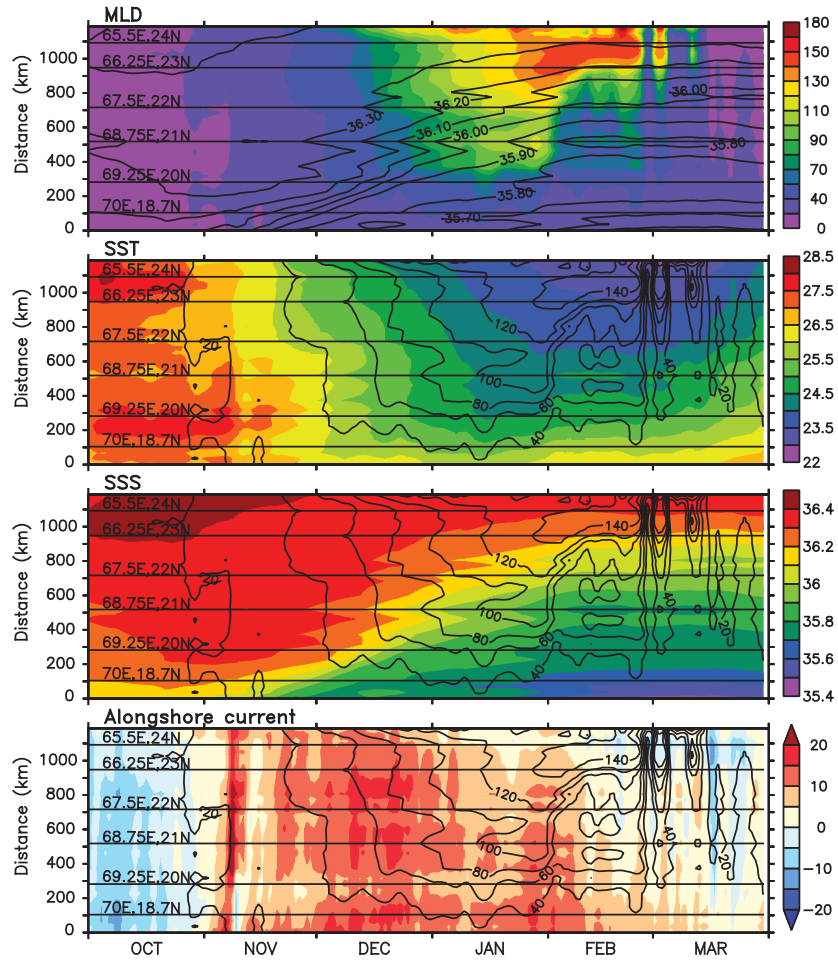


**Fig. 9** Variation during October–March of the model MLD (m, top panel), SST ( $^{\circ}\text{C}$ , second panel), SSS (psu, third panel), and alongshore current ( $\text{cm s}^{-1}$ , bottom panel; positive poleward) along the 1000 m isobath. The model grid cells used for these plots are marked in Figure 1. The abscissa is time and the ordinate gives the distance (in hundreds of kilometres) poleward along the 1000 m isobath from  $18^{\circ}\text{N}$ . The latitude and longitude are marked by horizontal lines. SSS contours are overlaid on the MLD panel and MLD contours are overlaid on the other three panels.

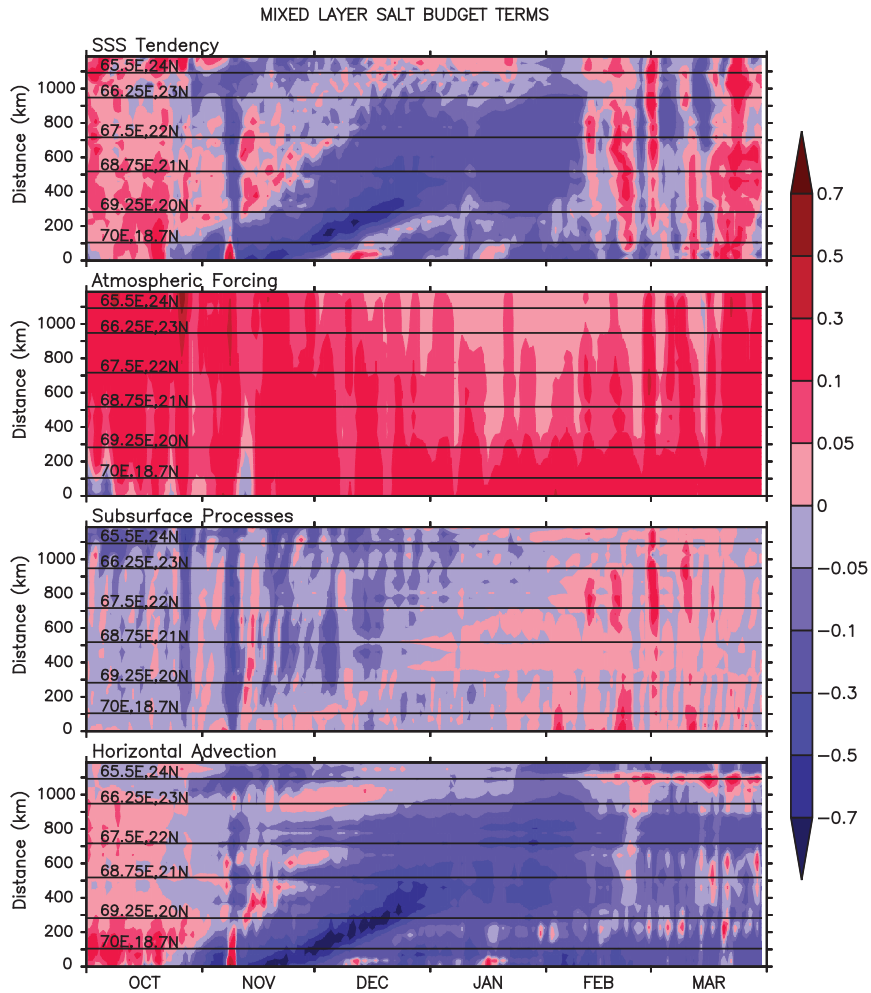


**Fig. 10** The ML salt budget during October–March. The tendency term (top panel) and the contributions of atmospheric forcing (second panel), sub-surface processes (third panel), and horizontal advection (bottom panel) are plotted along the 1000 m isobath. The unit is  $\text{psu month}^{-1}$  and the model grid cells used for these plots are marked in Figure 1. The sub-surface processes comprise vertical advection, entrainment, and turbulent processes (Vialard and Delecluse 1998; Kurian and Vinayachandran 2007). The abscissa is time and the ordinate gives the distance (in hundreds of kilometres) poleward from  $18^{\circ}\text{N}$ ; the latitude and longitude are marked by horizontal lines.

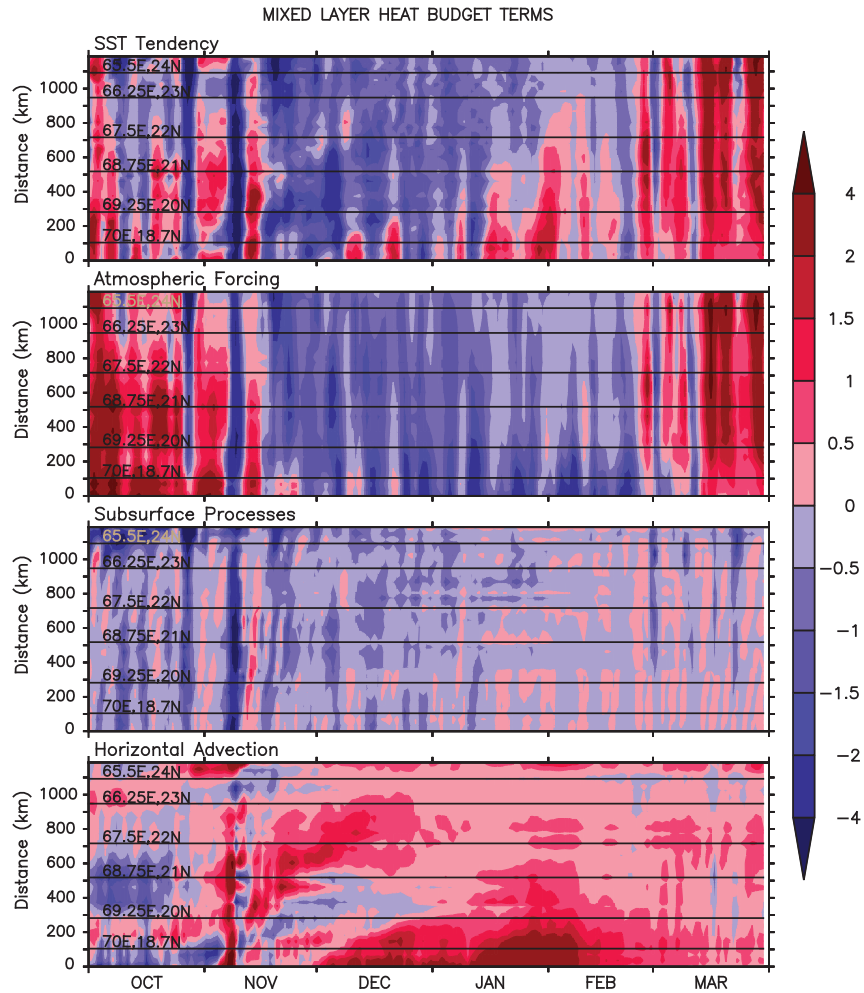


**Fig. 11** The ML heat budget during October–March. The tendency term (top panel) and the contributions of atmospheric forcing (second panel), sub-surface processes (third panel), and horizontal advection (bottom panel) are plotted along the 1000 m isobath. The unit is  $^{\circ}\text{C month}^{-1}$  and the model grid cells used for these plots are marked in Figure 1. The sub-surface processes comprise vertical advection, entrainment, and turbulent processes (Vialard and Delecluse 1998; Kurian and Vinayachandran 2007). The abscissa is time and the ordinate gives the distance (in hundreds of kilometres) poleward from  $18^{\circ}\text{N}$ ; the latitude and longitude are marked by horizontal lines.

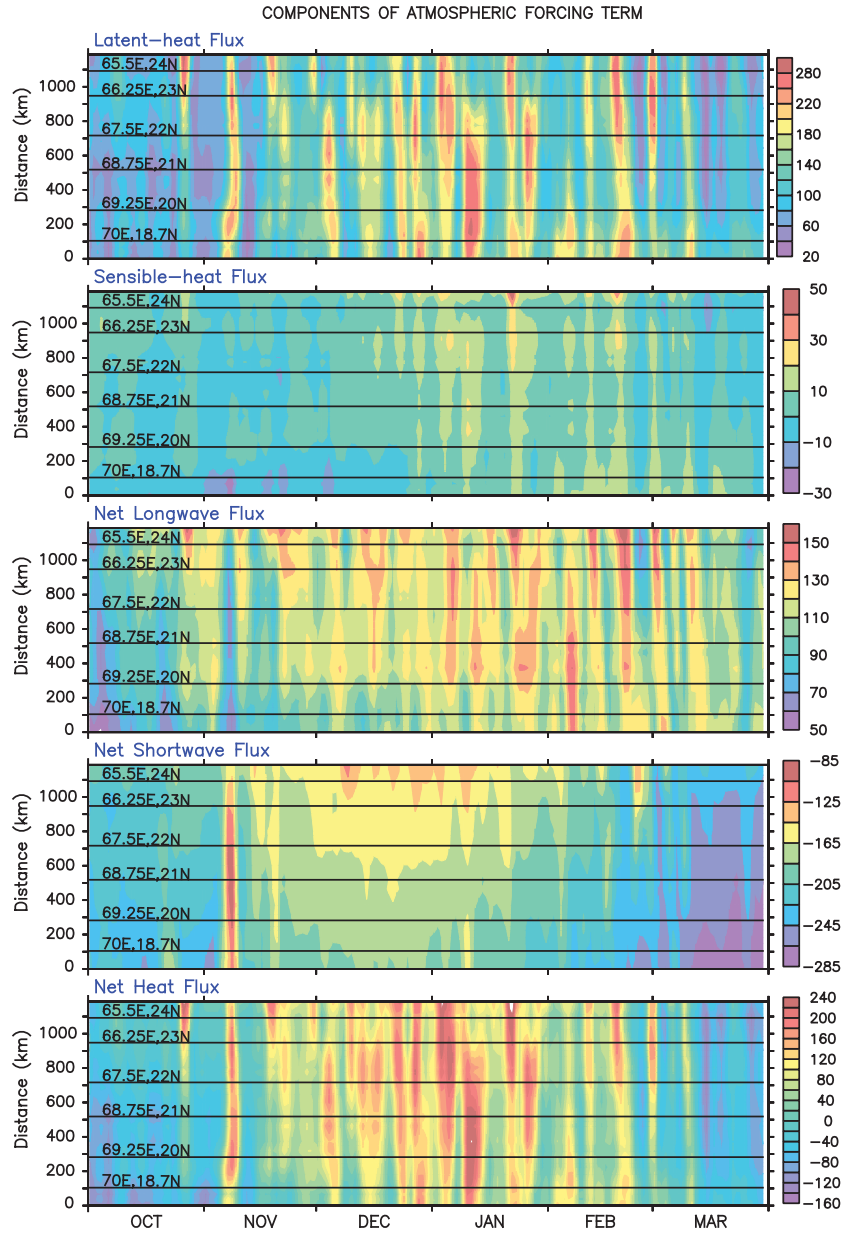


**Fig. 12** Contribution of components of the atmospheric-forcing term to the ML heat budget during October–March. The latent-heat flux (top panel), sensible-heat flux (second panel), net longwave flux (third panel), net shortwave flux (fourth panel), and net heat flux (bottom panel) are plotted along the 1000 m isobath. The unit is  $^{\circ}\text{C month}^{-1}$  and the model grid cells used for these plots are marked in Figure 1. Note that the colour scale is different for each term. The abscissa is time and the ordinate gives the distance (in hundreds of kilometres) poleward from  $18^{\circ}\text{N}$ ; the latitude and longitude are marked by horizontal lines.

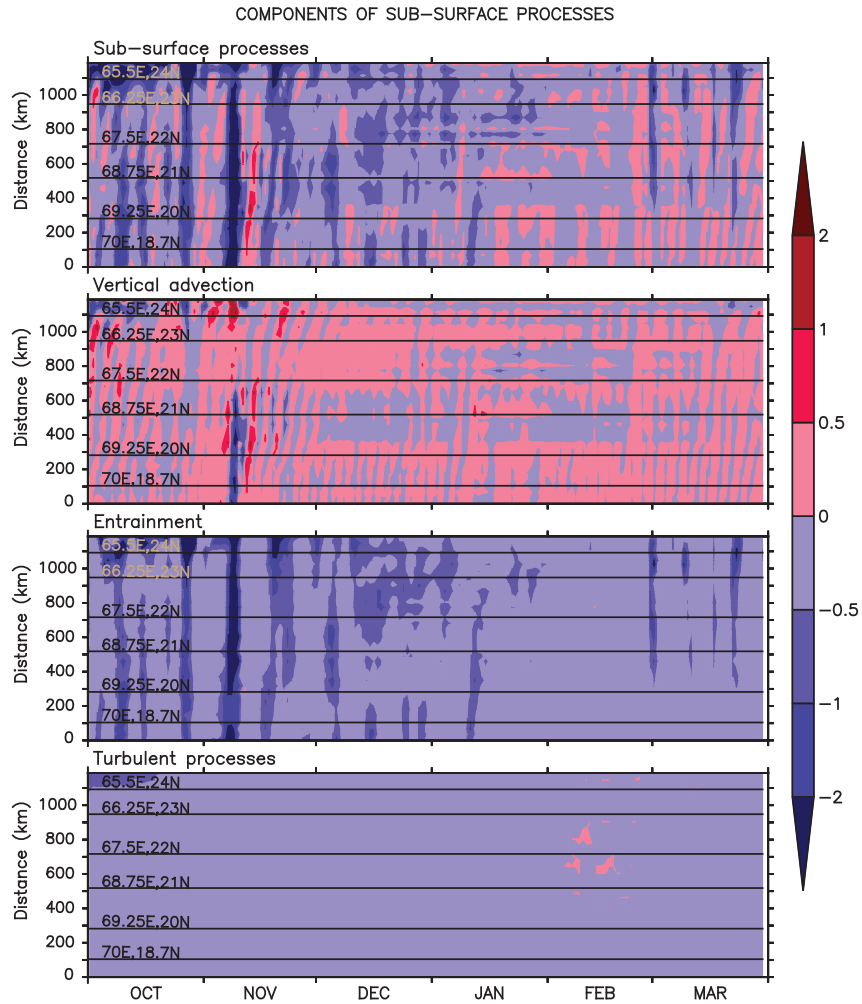


**Fig. 13** Contribution of components of the sub-surface processes to the ML heat budget during October–March. The sub-surface processes term (top panel) is plotted along the 1000 m isobath along with its components: vertical advection (second panel), entrainment (third panel), and turbulent processes (bottom panel). The unit is  $^{\circ}\text{C month}^{-1}$  and the model grid cells used for these plots are marked in Figure 1. The abscissa is time and the ordinate gives the distance (in hundreds of kilometres) poleward from  $18^{\circ}\text{N}$ ; the latitude and longitude are marked by horizontal lines.

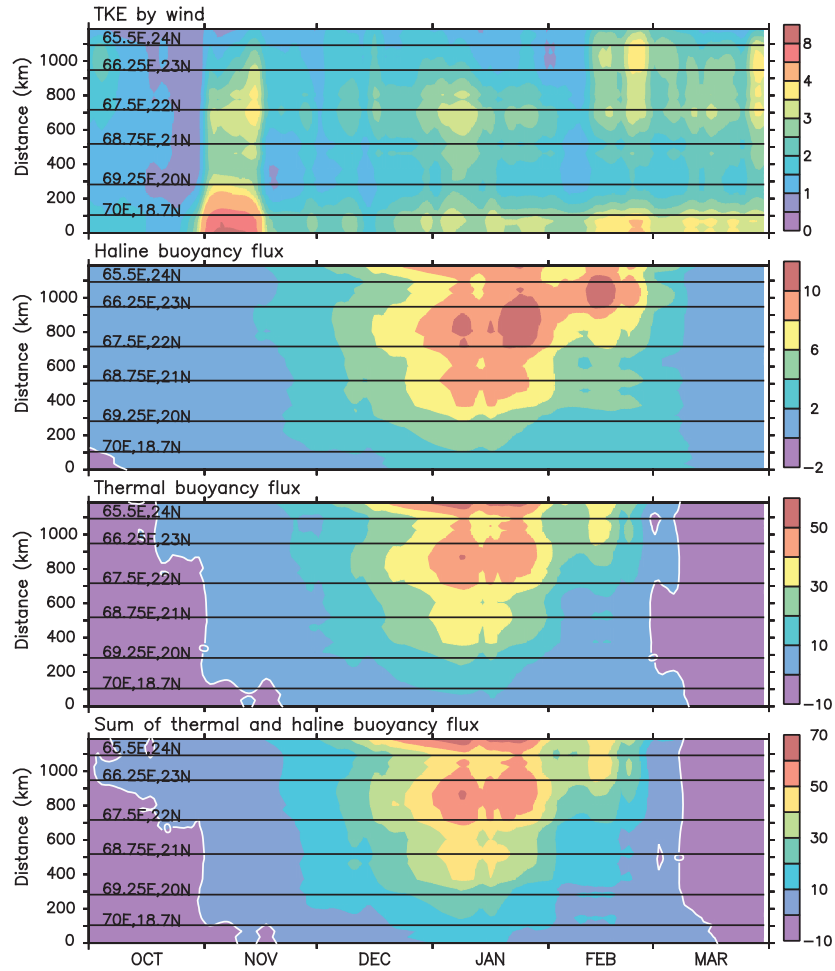


**Fig. 14** The turbulent kinetic energy input by the wind (top panel), haline buoyancy flux (second panel), thermal buoyancy flux (third panel), and the sum of thermal and haline buoyancy fluxes (bottom panel) along the 1000 m isobath during October–March. The unit is  $10^{-7} \text{ m}^3 \text{ s}^{-3}$  (the values have been multiplied by  $10^7$  before plotting) and the model grid cells used for these plots are marked in Figure 1. The thermal and haline buoyancy fluxes were smoothed with a 15-day running mean to damp the noise in the daily fields. The abscissa is time and the ordinate gives the distance (in hundreds of kilometres) poleward from  $18^\circ\text{N}$ ; the latitude and longitude are marked by horizontal lines.



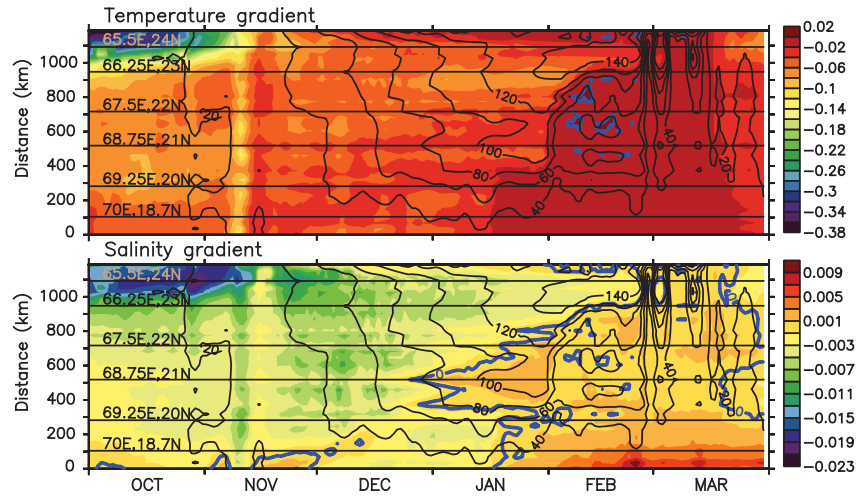


**Fig. 15** Temperature gradient ( $^{\circ}\text{C m}^{-1}$ , top panel) and salinity gradient ( $\text{psu m}^{-1}$ , bottom panel) at the base of the ML along the 1000 m isobath during October–March. The model grid cells used for these plots are marked in Figure 1. The abscissa is time and the ordinate gives the distance (in hundreds of kilometres) poleward from  $18^{\circ}\text{N}$ ; the latitude and longitude are marked by horizontal lines. The zero contour is shown (blue curve) and the MLD (m) contours (black curves) are overlaid.